Master's thesis

NTNU
Norwegian University of Science and Technology
Faculty of Engineering
Department of Civil and Environmental Engineering

Lars Ottar Jorde

Numerical investigation on scour around a cylinder and stabilities of scour protections

Master's thesis in Civil and Environmental Engineering
Supervisor: Hans Bihs
Co-supervisor: Ronja Ehlers and Weizhi Wang
June 2022

NTNU
Norwegian University of Science and Technology

Lars Ottar Jorde

Numerical investigation on scour around a cylinder and stabilities of scour protections

Master's thesis in Civil and Environmental Engineering
Supervisor: Hans Bihs
Co-supervisor: Ronja Ehlers and Weizhi Wang
June 2022

Norwegian University of Science and Technology
Faculty of Engineering
Department of Civil and Environmental Engineering

NTNU
Norwegian University of
Science and Technology

Abstract

A three-dimensional numerical model is used to investigate local scour around a cylinder in a rectangular flume under current. Numerical modelling of scour around a cylinder is challenging, since the required accuracy of the velocity field is not available due to computational capacity. Therefore, the numerical model must have approximations. The goal of this thesis is to investigate different parameters in the numerical setup in order to obtain a scour profile that fits the result of an experiment. The goal is also to examine the effect of scour protection in order to meet the challenges of future structures.

The chosen numerical model is calculated with a sediment transport model in REEF3D::CFD. The sediment transport model estimates the scour of sediments by calculating the bed shear stress. The initiation of motion begins when the bed shear stress exceeds the critical shear stress. The bed shear stress is calculated with several approaches, in which the formulation based on the turbulent kinetic energy resulted in the best contour of the bed surface. The sandslide algorithm determines the slope of the bed and redistributes the sediments if the slope exceeds the angle of repose. The effect of changing parameters such as the critical Shields parameter, shear stress reduction, equivalent sand roughness and suspended transport load are also presented in this thesis.

The numerical model are tested with increasing the diameter of the cylinder and adding scour protection. The diameter was increased to see if more elements surrounding the cylinder could influence the local scour. The results showed an enlarged depth and shape of the scour for cylinders with larger diameters. The scour protection was investigated with a simplified model solved with the sediment transport model. The result showed a clear pattern where the scour was reduced.

Acknowledgments

I would like to thank NTNU for five educational and challenging years in Trondheim. This master thesis would not be possible without Professor Hans Bihs, who built a knowledgeable team around me.

I am truly grateful for all the support from my co-supervisors PhD Candidate Ronja Ehlers and Researcher Weizhi Wang for all discussions, guidance and patience. Their expertise and availability has been irreplaceable.

Finally, I want to thank all the people in the reading room for a fun and motivating semester, my family for all the support and especially my brother for being an encouraging roommate.

Contents

List of Figures

Chapter 1

Introduction

Today's society is dependent on energy and the future will require even more energy. The world is becoming increasingly digital and needs more energy. Norway's power consumption this year is approximately 140 TWh according to Statnett's LMA. Statnett envisages three different scenarios for future power consumption in Norway. The scenarios give an annual energy needs in 2050 for 160 TWh, 190 TWh or 220 TWh depending on Norway's growth of energy requirement are moderate or high. The future demands more energy at the same time as the world is experiencing global warming.

Global warming is the long-term increased temperature in the climate system. Global warming is a consequence of many factors, but global energy-related emissions are one of the largest contributions by humans according to Masson-Delmotte and [eds.]. The total emission of CO_2 from energy sources has increased from 20.5 Gt in 1990 to 33.4 Gt in 2019, as given in IEA. The emission of CO_2 contributes to global warming and the consequence is presented in Figure 1.1 with different scenarios for future emission.

The scenarios presented in the figure show that CO_2 emissions must be reduced to zero by 2060 to limit an increase in temperature to 1.9 K. The world is facing a challenge where more energy is required at the same time as CO_2 emissions must be reduced. Therefore, the world must produce more renewable energy. Sun, wind and water are great sources of renewable energy. These renewable energy sources are already being used, but they must produce more energy in the future. The need for offshore wind turbines, floating solar and hydroelectric energy will increase in the future to meet the climate change. The Norwegian Government stated a major investment in offshore wind power for the future as shown in Gov. Norway has presented a plan where they want to facilitate the development of 1500 wind turbines by 2040. Wind turbines will produce up to 30 GW of renewable energy.

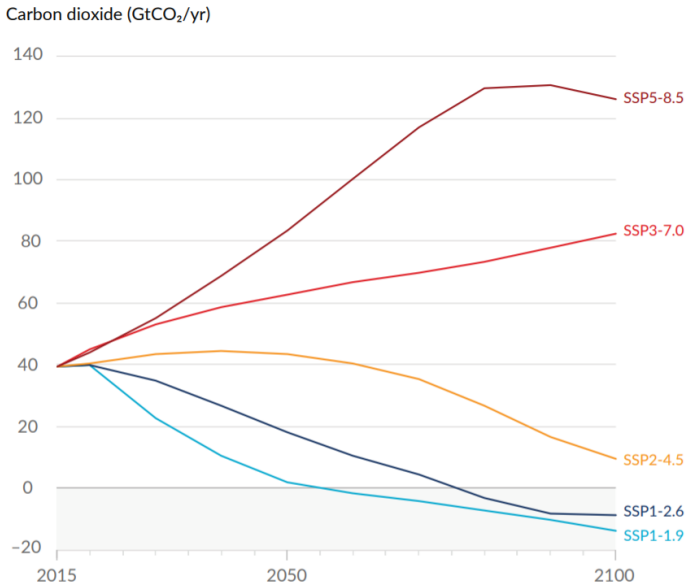

Figure 1.1: Present the increase of temperature for five different scenarios for future emission of CO_2. The scenarios give following rise in irreversible global temperature, $SSP1-1.9 = 1.9$ K, $SSP1-2.6 = 2.6$ K, $SSP2-4.5 = 4.5$ K, $SSP3-7.0 = 7.0$ K and $SSP5-8.5 = 8.5$ K. The figure is obtained from Masson-Delmotte and [eds.].

This corresponds to an annual production of 120 TWh which is approximately the annual consumption of electricity in Norway.

There are 1500 offshore wind turbines to be built in Norway, and there are many more in the world. Construction of offshore wind turbines requires knowledge of the intersection between soil, structure and water. Knowledge of the ground condition is acquired through expensive field investigations. Field investigations provide information that is used for necessary calculations to ensure sufficient stability in the ground.

Computational Fluid Dynamics (CFD) is a cost-effective tool to simulate the intersection between waves, soil and structure. Problems with scour around structures are a common challenge that can be calculated with a sediment model in CFD. CFD can provide cost-effective information about the intersection between soil, structure and water. Simulations with CFD will determine bed shear stress, velocity field, force on the structure from the water and more. Knowledge is the key to finding better and more creative solutions. This thesis will also try to investigate the effect of scour protection.

1.1 State-of-the-Art

1.1.1 Sediment transport

Sediment transport is initiated by the movement of water over rough sediments. The movement of water over the sediments creates bed shear stresses. The velocity distribution over depth for smooth and rough flows is presented in van Rijn [1993]:

$$\frac{u}{u_*} = \frac{1}{\kappa} ln(\frac{z}{z_0}) \quad where \quad z_0 = \frac{k_s}{30} \tag{1.1}$$

The shear velocity is u_*, u is the near-bed velocity at a height z, $\kappa = 0.4$ is the von Karman constant, k_s is equivalent sand roughness, d_{50} is the medium grain size. The bed shear stress is determined by the calculated shear velocity on the bed surface:

$$\tau = \rho_w u_*^2 \tag{1.2}$$

The transport of sediments begins when the bed shear stress exceeds the critical shear stress. The critical shear stress is determined as follows:

$$\tau_c = \theta_c * g(\rho_s - \rho_w) d_{50} \tag{1.3}$$

where ρ_s is the sediment density, ρ_w is the water density, g is the gravitational acceleration and θ_c is the Shields parameter from Shields [1936].

1.1.2 Earlier studies of CFD Models

Computational Fluid Dynamics (CFD) simulates the flow field by solving Reynolds-averaged Navier-Stokes (RANS) equations. The free surface is captured with the level-set method. The topography of the bed surface is calculated by looking at the movement of sediments with the sediment transport model. CFD models have the advantage of considering viscosity of fluid, rotational flow and turbulence when water interact with structures. A summary of previous studies on scour modelling using CFD modelling are presented below.

Olsen and Melaaen [1993] and Olsen and Kjellesvig [1998] were among the first to model scour with CFD. These studies investigated scour around a vertical pile exposed for a 3D flow based on Navier-Stokes equations with a turbulence model. The simulation captured the scour at selected times.

Brørs [1999] studied two dimensional scour around pipelines in current flow. Exner equations were used to determine the topography of the bed. Variation in scour depth

over time was included in this study. The free surface was replaced with a rigid lid, which limits the model to current with low flow.

Tseng et al. [2000] used 3D flow field to analyse the scour around square and circular piers. The interaction between the horseshoe vortex and the wake vortex was investigated and gave good results.

Li and Cheng [2001] looked into bed shear stress around pipeline using large eddy simulation model (LES). The equilibrium scour profile is calculated by a iterative method. The equilibrium scour profile assumes that the equilibrium bed shear stress is equal to the critical bed shear stress without the use of sediment transport formulas.

Roulund et al. [2005] examined the live-bed scour using 3D steady-state flow around a cylinder. The model did not solve the free surface which limits the study for currents with very low flow. The bed shear stress was reduced as the scour developed around the cylinder.

One of the first attempts of modelling scour under waves with CFD was investigated by Liang and Cheng [2005]. The model was a two-dimensional simulation of a pipeline. The model included the bed load and the suspended load in the sediment model with a different timescale for the flow field and morphological changes. The seabed morphology calculation is based on the period-averaged sediment transport rate with a morphological time step that is chosen by designating a maximum allowable bed deformation in each update. The waves are modelled as sinusoidal oscillatory flows without calculations of the free surface. The free surface impacts the scour when the change in the free surface is large compared to the water depth.

Liu and García [2008] investigated 3D numerical model of the local scour around a cylinder under waves where the free surface was included. The free surface was calculated by volume of fluid (VOF) scheme. The moving mesh method captured the interface between water and sediment.

Bihs and Olsen [2011] improved results of scour for numerical simulation of an abutment under current. The numerical simulation reduced the bed shear stress on a sloping bed by calculating a reduction factor. The most suitable reduction factor on a sloping bed was found by Kovacs and Parker [1994].

Fuhrman et al. [2014] described the backfilling process of sediments near a pipeline under waves. The backfilling process is characterised by an initial redistribution phase

involving reorganisation of sediments close to the pipeline and a longer backfilling process toward equilibrium scour depth.

Baykal et al. [2015] looked into a vertical pile under current. The result of the numerical model showed that the equilibrium scour depth was found to be reduced by 50% when the suspended load is not included.

Ahmad et al. [2015] simulated detailed flow field and sediment transport around a non-slender cylinder under regular waves. The level-set method was used to capture the free surface and geometric representation of the bed location. The convection term and the level-set method was discretised with the $5th$ order Weighted Essentially Non-Oscillatory scheme. The local scour was predicted for different KC numbers.

Ahmad et al. [2018] investigated wave-induced scour around piles in a side-by-side arrangement. The numerical model implemented a sandslide algorithm in the morphological model. The result was simulated with a full-size and a reduced-size NWT. The simulated result shows that the fully developed waves and the resulting scouring can be modelled in a reduced-length NWT with the same quality as in a full-sized NWT. Ahmad et al. [2019b] presents a numerical investigation on scour in front of a seawall. The study examined the impact of the breaking wave on a vertical seawall. Ahmad et al. [2019a] investigated scour around a pipeline under combined action of waves and current. The model solves the Reynolds-Averaged Navier-Stokes (RANS) equations together with the $k - \omega$ turbulence model and a sediment transport algorithm. The model calculates the scour under current and waves alone, followed by waves and currents combined. Ahmad et al. [2020] examined a numerical investigation of local scour around a jacket structure with dynamic free surface capture. The modelling of flow hydrodynamics and the time development of local scour around a jacket exposed to waves and steady current where the key findings.

Liu et al. [2016] considered scour under waves around pipelines using a nonlinear wave model. The free surface and the intersection between sediment and water were tracked using the Arbitrary Lagrangian-Eulerian (ALE) method.

1.2 Objectives of the study

Numerical modelling of scour around vertical cylinders has been done several times before. This thesis will investigate the critical parameters for the development of scour under currents and investigate the effect of scour protection. The objectives of the study are the following:

- Validate the numerical wave tank for wave propagation and interaction with a cylinder.
- Investigate the sediment transport model with a parameter study.
- Investigate the effect of scour protection.

Chapter 2

Numerical model

2.1 Governing Equations

Computational fluid dynamics (CFD) uses three-dimensional Reynolds-Averaged Navier-Stokes equations (RANS) to calculate the fluid flow. RANS equations are based on the assumption that the fluid is a continuum and are solved by the conservation laws for mass and momentum:

$$\frac{\partial u_i}{\partial x_i} = 0 \tag{2.1}$$

$$\frac{\partial u_i}{\partial t} + u_j \frac{\partial u_i}{\partial x_j} = -\frac{1}{\rho}\frac{\partial p}{\partial x_i} + \frac{\partial}{\partial x_j}\left[(\nu + \nu_t)\left(\frac{\partial u_i}{\partial x_j} + \frac{\partial u_j}{\partial x_i}\right)\right] + g_i \tag{2.2}$$

where u is the velocity averaged over time t, ρ is the fluid density, p is the pressure, ν is the kinematic viscosity, ν_t is the eddy viscosity and g the gravitational acceleration.

The model uses advanced finite difference methods for approximating the spatial derivatives on a Cartesian grid. The convective terms of the momentum equations are discretized with the conservative Weighted Essential Non-oscillatory (WENO) scheme of fifth-order accuracy presented in Jiang and Shu [1996]. The third-order TVD Runge-Kutta time scheme presented in Shu and Osher [1988] is used for the time treatment of the momentum equations, the level-set function and the reinitialisation equations. The numerical time step for the transient flow field is determined using adaptive time steps, where the time step is controlled using the Courant-Friederichs-Lewy (CFL) number from Griebel et al. [1998], which takes into account the influence of velocity, diffusion and source terms, such as acceleration due to gravity. In a RANS model, the diffusion criterion can become restrictive, and therefore it is treated implicitly to remove it from the CFL criterion described in Bihs et al. [2016]. The projection method in Chorin [1968] describes the pressure. The BiCGStab (van der Vorst [1992]) solver from the high-performance solver package HYPRE with the semi-coarsening

multi-grid preconditioner PFMG (Ashby and Falgout [1996]) is implemented to solve the Poisson equation for pressure.

2.2 Turbulence Model

2.2.1 $k-\omega$ Model

The $k-\omega$ model is the most popular two-equation turbulence model and described in [Wilcox et al., 1994]:

$$\frac{\partial k}{\partial t} + u_j \frac{\partial k}{\partial x_j} = \frac{\partial}{\partial x_j}\left[\left(\nu + \frac{\nu_t}{\sigma_k}\right)\frac{\partial k}{\partial x_j}\right] + P_k - \beta_k k\omega \tag{2.3}$$

$$\frac{\partial \omega}{\partial t} + u_j \frac{\partial \omega}{\partial x_j} = \frac{\partial}{\partial x_j}\left[\left(\nu + \frac{\nu_t}{\sigma_\omega}\right)\frac{\partial \omega}{\partial x_j}\right] + \frac{\omega}{k}\alpha P_k - \beta\omega^2 \tag{2.4}$$

The model is consisting of the turbulent kinetic energy k and the specific turbulent dissipation ω. P_k is the turbulent production rate defined as:

$$P_k = \nu_t \frac{\partial u_i}{\partial x_j}\left[\frac{\partial u_i}{\partial x_j} + \frac{\partial u_j}{\partial x_i}\right] \tag{2.5}$$

The coefficients have the values $\alpha = \frac{5}{9}$, $\beta_k = \frac{9}{100}$, $\beta = \frac{3}{40}$, $\sigma_k = 2$ and $\sigma_\omega = 2$.
In oscillatory flow, the eddy viscosity is limited to avoid overproduction of turbulence in highly strained flow outside the boundary layer. In Durbin [2009] the eddy viscosity ν_t is limited to the following:

$$\nu_t = \min\left(\frac{k}{\omega}, \sqrt{\frac{2}{3}}\frac{k}{|\mathbf{S}|}\right) \tag{2.6}$$

where $\mathbf{S}$ is the mean strain rate:

$$S_{ij} = \left(\frac{\partial u_j}{\partial x_i} + \frac{\partial u_i}{\partial x_j}\right) \tag{2.7}$$

2.3 Free surface model

2.3.1 Level Set Method

The level set method describes the interfaces between water and air which is used to capture the free surface. The location of the free surface level is represented by the distance function $\phi(\vec{x}, t)$ from Osher and Sethian [1988]:

$$\phi(\vec{x},t)\begin{cases} > 0 \; if \; \vec{x} \in phase \; 1 \\ = 0 \; if \; \vec{x} \in \Gamma \\ < 0 \; if \; \vec{x} \in phase \; 2 \end{cases} \tag{2.8}$$

The level set function is calculated from RANS equations for the velocity field u_j:

$$\frac{\partial \phi}{\partial t} + u_j \frac{\partial \phi}{\partial x_j} = 0 \tag{2.9}$$

Numerical difficulties will appear near the interface due to sharp changes in the fluid density ρ and the eddy viscosity ν_t. The numerical difficulties are solved by smoothening over a length ϵ on both sides of the interface using a Heaviside function $H(\phi)$. The density ρ and viscosity ν near the interface are:

$$\begin{aligned} \rho &= \rho_1 H(\phi) + \rho_2 (1 - H(\phi)), \\ \nu &= \nu_1 H(\phi) + \nu_2 (1 - H(\phi)) \end{aligned} \tag{2.10}$$

where the Heaviside function defined as:

$$H(\phi) = \begin{cases} 0 & if \; \phi < -\epsilon \\ \frac{1}{2}\left(1 + \frac{\phi}{\epsilon} + \frac{1}{\pi} sin\left(\frac{\pi\phi}{\epsilon}\right)\right) & if \; |\phi| < \epsilon \\ 1 & if \; \phi > \epsilon \end{cases} \tag{2.11}$$

Typically the length of the smoothening distance is chosen to be $\epsilon = 1.6$ dx on both sides of the interface.

2.3.2 Reinitialization

The level set function can loose its signed distance property when the interface evolves under external velocity field. The level set function need to be reinitialized in order to obtain accuracy of the interface. A PDE based reinitialization equation is solved from Sussman et al. [1994]:

$$\frac{\partial \phi}{\partial t} + S(\phi)\left(\left|\frac{\partial \phi}{\partial x_j}\right| - 1\right) = 0 \tag{2.12}$$

where $S(\phi)$ is the smoothed sign function by Peng et al. [1999].

2.3.3 Sediment transport model

The sediment transport model calculates the sediment transport and changes of the bed topography. The governing equation of the bed changes is defined as:

$$\frac{\partial z_b}{\partial t} + \frac{\partial q_{T_x}}{\partial x} + \frac{\partial q_{T_y}}{\partial y} = 0 \tag{2.13}$$

where z_b is the vertical location of the bed and q_T is the total-load sediment in the bed cell. The sediment transport is captured by bed load transport and suspended load transport.

Bed load Transport

The bed load transport can be calculated from several approaches. This master thesis are considering the approaches from Engelund and Fredsøe [1976] and van Rijn [1984]. The bed load q_b^* solved with the bed load formula from Engelund and Fredsøe [1976]:

$$q_{b,i}^* = \begin{cases} 0 & if\ \tau^* < \tau_{c,i}^* \\ 18.74\left(\tau^* - \tau_{c,i}^*\right)\left(\tau^{*0.5} - 0.7\tau_{c,i}^{*0.5}\right) & if\ \tau > \tau_{c,i}^* \end{cases} \tag{2.14}$$

where

$$\tau_{c,i}^* = \frac{\tau_{c,i}}{(\rho_s - \rho)\, g d_i} \tag{2.15}$$

The density of sediment is ρ_s, the density of water is ρ, the gravitational acceleration is g, and the diameter of the sediment particle is d_i. The dimensionless bed load transport rate is $q_{b,i}^*$ and the dimensionless critical shear stress is $\tau_{c,i}^*$. The dimensionless bed shear stress is τ^*. The critical bed shear stress τ_c is calculated in Eq. 1.3. The critical shear stress is reduced for sloping bed shown in section 2.3.3.

The bed load q_b calculated with bed load formula from van Rijn [1984]:

$$\frac{q_b}{d^{1.5}\sqrt{\frac{(\rho_s-\rho_w)*g}{\rho_s}}} = 0.053 * \frac{\left(\frac{\tau-\tau_c}{\tau_c}\right)^{2.1}}{\left(d\,\frac{\rho_s/(\rho_w-1)*g}{\nu^2}\right)^{1/3}}^{0.3} \tag{2.16}$$

where τ_c is the critical bed shear stress. The bed shear stress is τ, ρ_s is the sediment density, ρ_w is the water density, g is the gravitational acceleration, d is the diameter of the sediment particle and ν is the kinematic viscosity of the water.

Suspended Load Transport

The governing equation for suspended load is a standard convection-diffusion equation:

$$\frac{\partial c}{\partial t} + u_j \frac{\partial c}{\partial x_j} + w_s \frac{\partial c}{\partial z} = \frac{\partial}{\partial x_j}\left(\Gamma \frac{\partial c}{\partial x_j}\right) \tag{2.17}$$

where ω_s is the fall velocity of the sediment particles, c is the suspended load concentration and Γ is the diffusion coefficient which is assumed to be equal to the eddy viscosity given in Hunt and Inglis [1954].
The boundaries for this equation is zero sediment flux in vertical direction at the free surface and the concentration of sediment in the bed cells are calculated with the suspended load formula from van Rijn [1984b]:

$$c_b = 0.015 \frac{d_i}{a} * \frac{\left(\frac{\tau - \tau_{c,i}}{\tau_{c,i}}\right)^{1.5}}{\left(d_i \frac{\rho_s/(\rho_w - 1) * g}{\nu^2}\right)^{1/3}\Bigg)^{0.3}} \tag{2.18}$$

where a is the distance from the bed to the point, τ_c is the critical bed shear stress, τ is the bed shear stress, ρ_s is the density of the sediment, ρ_w is the density of the water, g is the gravitational acceleration, d is the sediment particle diameter and ν is the kinematic viscosity of water.

Morphological Model

The bed level changes are determined by using the sediment mass-balance for the cells closest to the bed:

$$(1 - p') \frac{\partial z_b}{\partial t} = -\frac{\partial q_{B_x}}{\partial x} - \frac{\partial q_{B_y}}{\partial y} - E_{susp} + D_{susp} \tag{2.19}$$

where p' is the porosity of the bed material, z_b is the elevation of the local bed, E_{susp} is the erosion rate, D_{susp} is the deposition rate and q_B is the bed load sediment in the bed cell that are given in the direction x and y direction. The elevation of the local surface of the bed z_b can be calculated by determining the other parameters with formulas for the bed load and the suspended sediment load.

Incipient Motion on a Sloping Bed

The critical bed shear stress τ_c shown in Eq. 1.3 is not considering the effect of the sloping bed. The longitudinal θ and transverse α angles on a sloping bed cell are given in Figure 2.1. The critical bed shear stress is reduced with a reduction factor

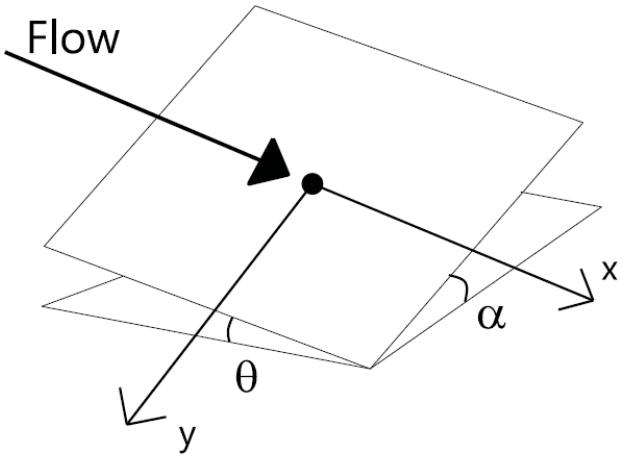

Figure 2.1: Illustrate the longitudinal θ and transverse α angles on a sloping bed cell, from Bihs [2011]

due to the sloping bed in Eq. 2.20. There are several approaches for the reduction factor, where only a few of them are presented in this thesis.

$$\tau_c = r * \tau_{c,Shield} \tag{2.20}$$

Fredsoe and Deigaard [1992] present a reduction factor that is limited to slopes with angle α perpendicular to the flow direction and depend on the angle of repose ϕ. The formula for reducing bed shear stress is as follows:

$$r = \sqrt{1 - \frac{tan^2\alpha}{tan^2\phi}} cos\alpha \tag{2.21}$$

Dey [2001] described an empirical equation that included the transverse angle α, the longitudinal angle θ and the angle of repose ϕ. The expression is given as:

$$r = 0.954 \left(1 - \frac{\theta}{\phi}\right)^{0.745} \left(1 - \frac{\alpha}{\phi}\right)^{0.372} \tag{2.22}$$

Dey [2003] determined also an analytical formula which included the ratio $\eta = F_L/F_D$ where F_L is the lifting force and F_D is the drag force:

$$\begin{aligned} r =& \frac{1}{(1-\eta tan\phi)\, tan\phi} \Bigg\{ -\left(sin\theta + \eta tan^2\phi\sqrt{cos^2\theta - sin^2\alpha}\right) \\ &+ \Bigg[\left(sin\theta + \eta tan^2\phi\sqrt{cos^2\theta - sin^2\alpha}\right)^2 \\ &+ \left(1-\eta^2 tan^2\phi\right)\left(cos^2\theta tan^2\phi - sin^2\alpha tan^2\phi - sin^2\theta - sin^2\alpha\right) \Bigg]^{0.5} \Bigg\} \end{aligned} \tag{2.23}$$

Kovacs and Parker [1994] determined a vectorial equation for the threshold for a combined transverse and longitudinal sloping bed. The equation was analytically solved as a quadratic equation by Seminara et al. [2002]:

$$\begin{aligned} &(1-\Delta)\, r^2 + 2\left(\frac{\Delta}{\sqrt{1+tan^2\theta+tan^2\alpha}} + \frac{sin\theta}{tan\phi}\right) r \\ &+ \frac{1+\Delta}{1+tan^2\theta+tan^2\alpha}\left(\frac{tan^2\theta+tan^2\alpha}{tan^2\phi} - 1\right) = 0 \end{aligned} \tag{2.24}$$

where Δ is approximated with $\eta tan\phi$ and describe the effect of the lifting force. The η are the ratio between the lift force and the drag force.

Sandslide Model

The sandslide algorithm combines the slope of the bed and the material property ϕ, which are the angle of repose. When the slope of the bed becomes larger than ϕ, the bed cells redistribute the sediment volume. This process continues until the slope of the bed is equal or less than ϕ.

Burkow [2010] calculate the slope of the bed by looking at the slope of each cell. The cell has eight possible neighbors where four is located at the edges and four at the corners. The sandslide algorithm controls the slope from the middle of the cell to the neighbors in the formulas given by Burkow [2010]:

$$\begin{aligned} |z_{i,k} - z_{i\pm1,k}| &< tan(\phi) * \Delta x \\ |z_{i,k} - z_{i,k\pm1}| &< tan(\phi) * \Delta y \\ |z_{i,k} - z_{i\pm1,k\pm1}| &< tan(\phi) * \Delta xy \end{aligned} \tag{2.25}$$

where z is the height of the sediment surface, ϕ is the angle of repose, Δx and Δy is the length to the edges and $\Delta xy = \sqrt{(\Delta x)^2 + (\Delta y)^2}$ is the length to the corners. The volume of sediments is redistributed to the neighbor cell when the slope of the

cell exceeds the angle of repose.

Wu [2007] calculate the slope of the bed by looking at the slope between the centers of two cells. The sandslide model is based on the inclination between the center of the cell and the center of the neighbor cell. The inclination is presented in figure 2.2.

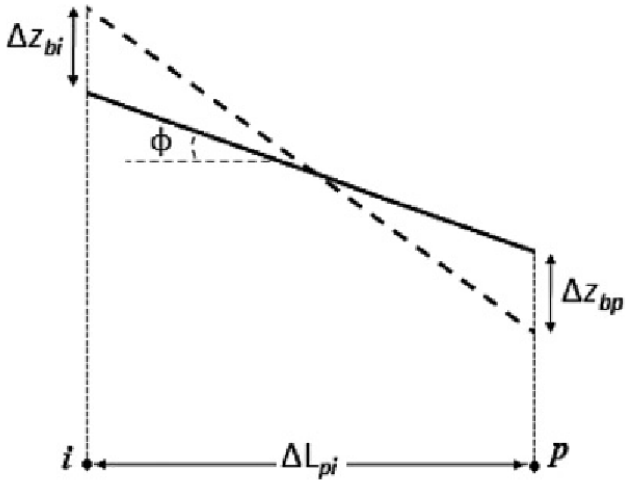

Figure 2.2: Definition of quantities involved in the sandslide algorithm used to adjust the computed bed slope. Dashed line show bedslope before and bold lines show bed slope after sandslide. Figure is obtained from Khosronejad et al. [2011]

Figure 2.2 shows the change in bed surface in cell P, Δz_{bP}, and in cell i, Δz_{bi}, over a length ΔL_{iP}. The sandslide algorithm described by Wu [2007] is given by:

$$(z_{bP} + \Delta z_{bP}) - (z_{bi} + \Delta z_{bi}) < tan(\phi) * \Delta L_{iP} \tag{2.26}$$

The mass will be reorganized to neighbor cells if the slope of the bed exceeds the angle of repose. The reorganization is to balance the mass between the bed cell P and the four neighbor cells with a formula given by Wu [2007]:

$$A_{hP} * \Delta z_{bP} - \sum_{i=1,2,3,4} A_{hi} * \Delta z_{bi} = 0 \tag{2.27}$$

where A_{hP} is the projection of the bed cell P and A_{hi} is the projection of the bed cell i.

2.4 Wave generation and absorption

The wave generation in the NWT is managed with relaxation method 2 and the Dirichlet-type boundary condition. Waves are generated by prescribing the horizontal and vertical velocity with the free surface elevation based on the level-set function. The computational values for the horizontal and vertical velocities in the numerical beach are smoothly reduced to zero. The free surface is reduced to the still water level and the pressure is relaxed to the hydrostatic pressure in the numerical beach. The numerical beach absorbs all the wave energy and prevents wave reflections. The relaxation domains are as follows:

$$\begin{aligned} u(\widetilde{x})_{relaxed} &= \Gamma(\widetilde{x})u_{analytical} + (1-\Gamma(\widetilde{x}))u_{computational} \\ w(\widetilde{x})_{relaxed} &= \Gamma(\widetilde{x})w_{analytical} + (1-\Gamma(\widetilde{x}))w_{computational} \\ p(\widetilde{x})_{relaxed} &= \Gamma(\widetilde{x})p_{analytical} + (1-\Gamma(\widetilde{x}))p_{computational} \\ \phi(\widetilde{x})_{relaxed} &= \Gamma(\widetilde{x})\phi_{analytical} + (1-\Gamma(\widetilde{x}))\phi_{computational} \end{aligned} \tag{2.28}$$

where the relaxation function presented in Jacobsen et al. [2012] is used:

$$\Gamma(\widetilde{x}) = 1 - \frac{e^{(\widetilde{x}^{3.5})} - 1}{e-1} \; for \; \widetilde{x} \in [0;1] \tag{2.29}$$

The coordinate $\widetilde{x}$ is scaled to the length of the relaxation zone. Several wave theories are implemented in REEF3D: linear waves, $2nd$ order and $5th$ order Stokes waves, $1st$ order and $5th$ order cnoidal waves, $1st$ order and $5th$ order solitary waves, and first order irregular and focused waves. In this way, the relaxation method employs different wave theories to generate different waves based on the wave type selected by the user.

Chapter 3

Numerical verification

The numerical wave tank will be verified in this section. The NWT will be tested with several simulations with different grid sizes. The purpose is to do a grid convergence study for different waves. Intermediate waves are certified with linear wave theory and $2nd$-order Stokes wave theory. Deep waves are tested for $2nd$-order Stokes wave theory. The grid convergence study is used to find the optimal grid size for obtaining an accurate result which demand as little as possible computational power.

The NWT is tested for the change in the free surface over a submerged bar exposed to nonlinear waves. The result presents how the free surface is affected by the submerged bar. The change in free surface is a consequence of the interaction between the waves and the submerged bar. The experiment is performed in Beji and Battjes [1993].

The force acting on a vertical cylinder is validated in a NWT. The cylinder are exposed to $2nd$-order Stokes intermediate waves. The experiment are carried out in Chen et al. [2014].

3.1 Numerical Wave Tank

The NWT is performed as a two-dimensional case. The length is 30 m and the width is limited to a single grid size, dx. The depths of the water vary due to the limitations of intermediate or deep waves. The wave generation zone is equal to one wavelength, and for the relaxation zone a length of two wavelengths is used. The calculated elevation of the free surface are compared with the theoretically free surface elevation for the chosen wave theory.

3.1.1 Intermediate linear waves

A grid convergence study is performed for intermediate waves with linear wave theory (LWT). The wavelength is 4 m and the water depth is 0.5 m. The results are presented in Figure 3.1. The figure shows the change in elevation of the free surface over time for different grid sizes located in the middle of the NWT. Calculations with CFD result in a more accurate free surface when the grid size is smaller. A smaller grid size in the NWT produces more elements that capture the free surface. The grid convergence is simulated for grid sizes $dx = 0.2$ m, $dx = 0.1$ m, $dx = 0.05$ m and $dx = 0.025$ m which are illustrated in Figure 3.1. The consequence of using a mesh with a small grid size is a longer simulation time. The simulated wave elevation from Figure 3.1 is converging against the theoretical solution for a grid size smaller than $dx = 0.05$ m. The numerical solution shows better accuracy for a grid size smaller than $dx = 0.5$ m, which validates this numerical model.

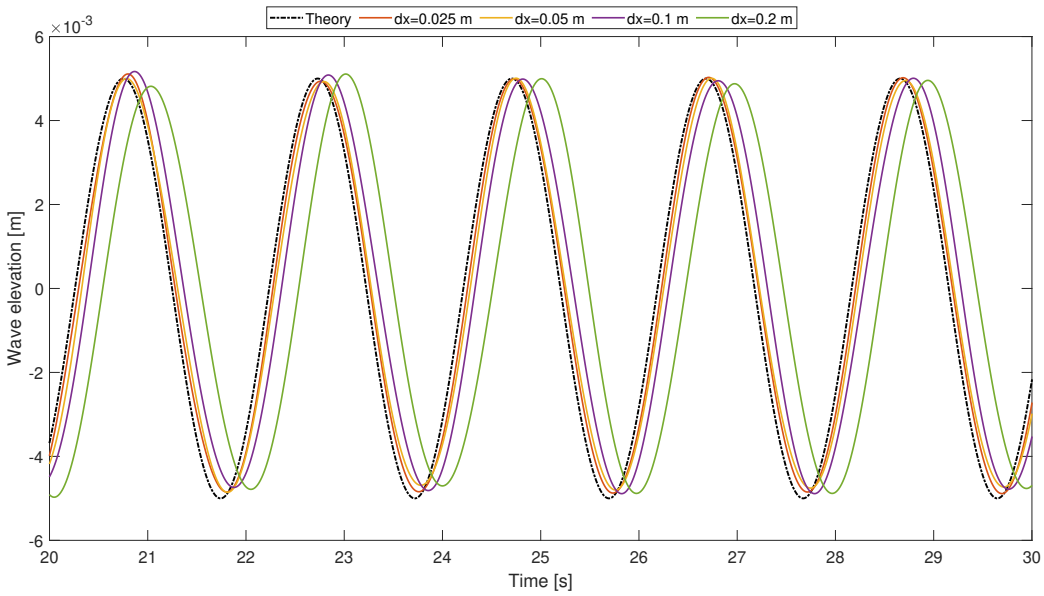

Figure 3.1: Grid convergence study for intermediate linear waves

3.1.2 Intermediate nonlinear waves

The numerical model in this case is solved with 2*nd*-order Stokes wave theory. The wavelength is 4 m and the depth of the water is 0.5 m. The grid convergence study is presented in Figure 3.2 for grid sizes $dx = 0.2$ m, $dx = 0.1$ m, $dx = 0.05$ m and $dx = 0.025$ m. The figure shows the change in elevation of the free surface over time located in the middle of the NWT. The wave elevation converges against the

theoretical solution for grid sizes smaller than $dx = 0.05$ m. The result proves that the NWT calculated with CFD converges against the theoretical solution for simulations with smaller grid sizes.

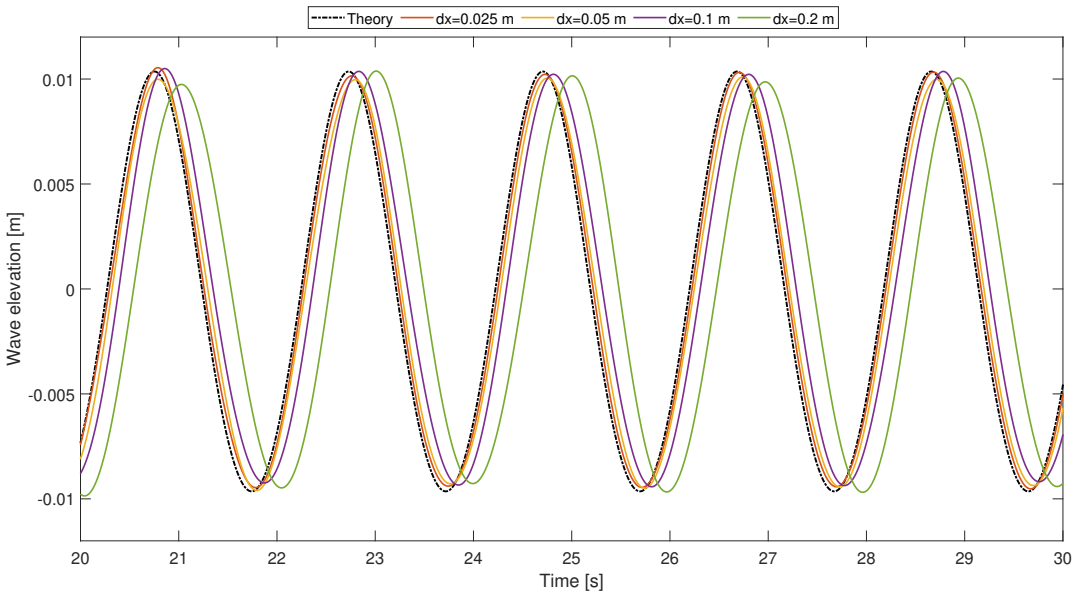

Figure 3.2: Grid convergence study for intermediate 2*nd*-order Stokes waves

3.1.3 Deep nonlinear waves

The deep waves are calculated with 2*nd* order Stokes wave theory. The wavelength is 4 m and the depth of the water is 2 m. The results of the convergence study are given in Figure 3.3. The figure shows the change in the free surface over time for different grid sizes located in the middle of the NWT. The wave height of the calculated solution in REEF3D converges against the theoretical solution with a finer mesh than $dx = 0.05$ m. The NWT is valid for deep nonlinear waves for simulations with a finer mesh than $dx = 0.05$ m.

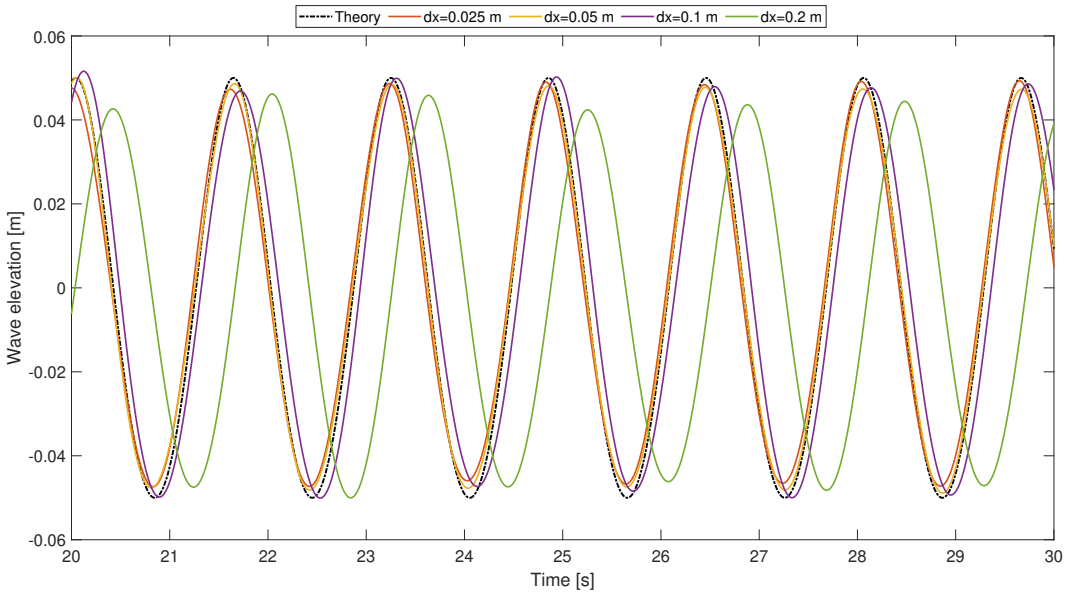

Figure 3.3: Grid convergence study for deep 2*nd* order Stokes waves

3.2 Wave Propagation over a Submerged Bar

A numerical model with a change in bathymetry will be validated by investigating the propagation of the wave over a submerged bar in a NWT. The numerical results of the two-dimensional submerged bar are compared with the experimental data from Beji and Battjes [1993]. The numerical setup is therefore 24 m long and one grid size wide. The chosen grid size is $dx = 0.1$ m. The depth of the water is 0.4 m and the wave length is $\lambda = 3.73$ m. The submerged bar changes the depth of the water from 0.4 m to 0.1 m shown in figure 3.4. The experiment contains wave gauges from several positions along the submerged bar. Wave gauges measure the free surface in the experiment. The results from the experiment are compared with the free surface calculated in the numerical simulation. The positions of the gauges are shown in Figure 3.4. The results of the validation are given in Figure 3.5.

Wave gauge 1 shows a great fit between the experimental and numerical result. The waves follow a smooth cosinus curve, since wave gauge 1 is located before the submerged bar. The same patterns are shown for the second wave gauge, but the wave heights increase while the wave reaches the submerged bar. Wave gauge 3 is located at the top of the submerged bar and the waves are very steep. The waves are so steep that they are generating new small waves. The new wave is gradually developing from wave gauges 3, 4 and 5. The numerical result shows a good fit to the experiment while the new wave develops. In wave gauges 6 and 7 are the water depth increasing and the wave height decreasing. The REEF3D solution has

small deviations from the experimental data in the nonlinear parts of the waves. The numerical model is still able to calculate the right size and form of wave propagation over the submerged bar with good accuracy.

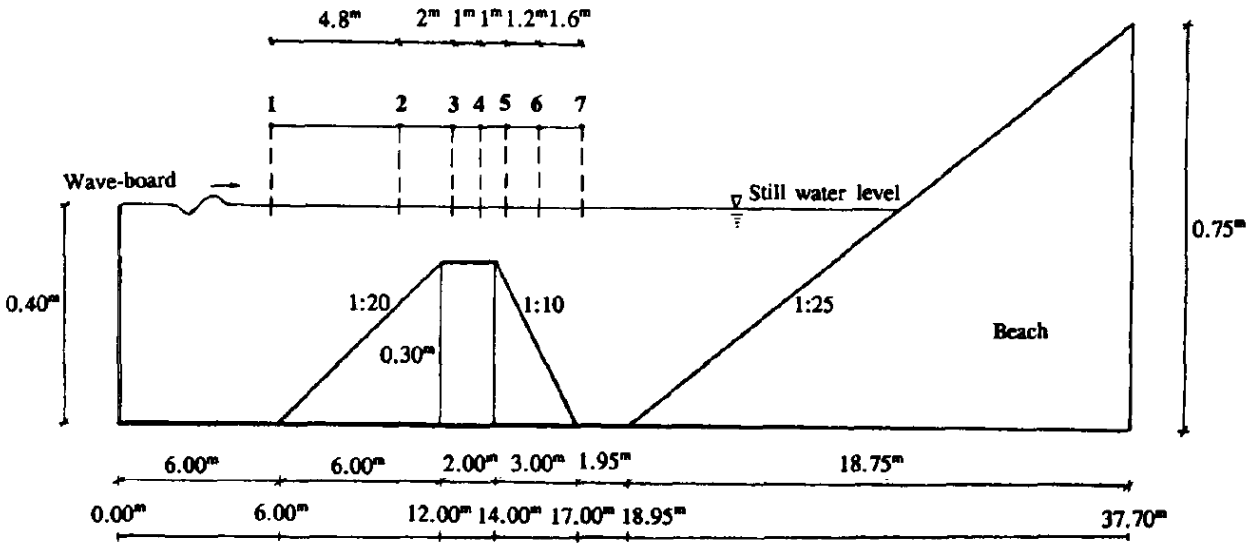

Figure 3.4: Numerical setup for the simulation of wave propagation over a submerged bar obtained from Beji and Battjes [1994]

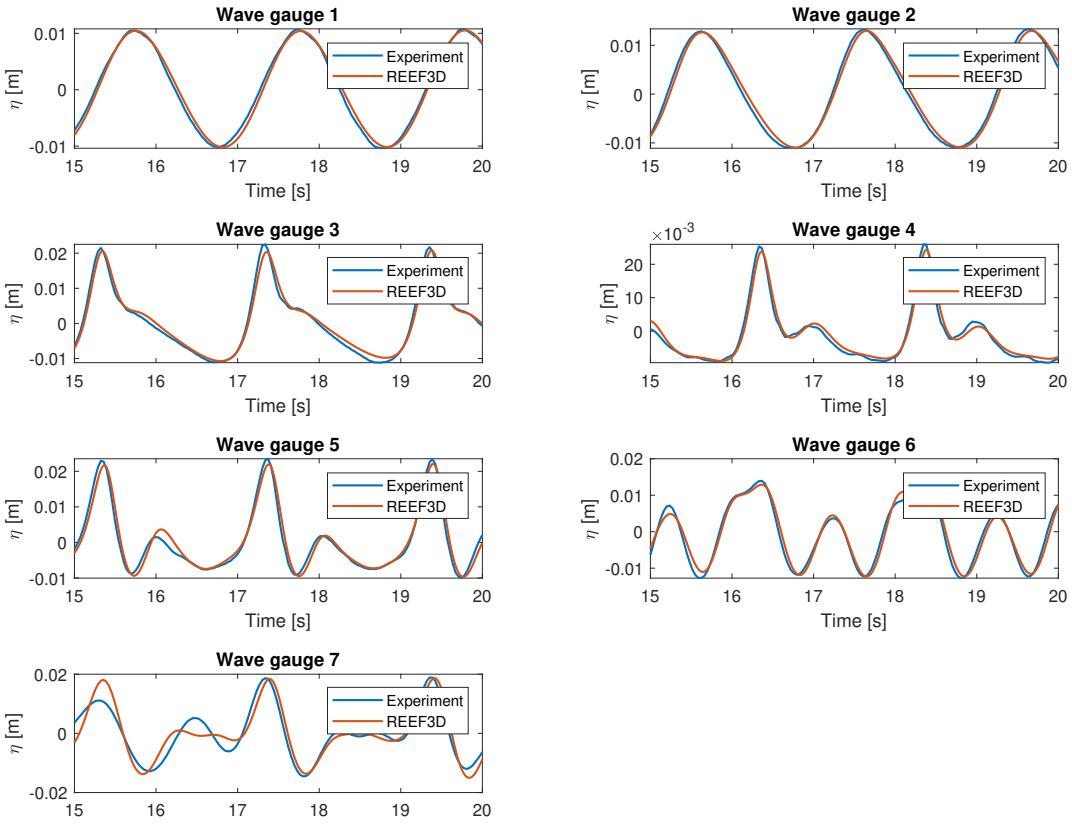

Figure 3.5: Wave gauges 1-7

3.3 Wave forces

The wave forces on a pile are used to verify the calculation of wave forces in the NWT by REEF3D::CFD. The results of the calculations will be compared with experimental data from Chen et al. [2014]. The numerical wave tank is 18 m long, 3 m wide and the pile has a diameter equal to 0.25 m. The numerical setup is given in Figure 3.6.

The results are given by a wave gauge in front of the pile. The wave gauge measures the wave elevation and the wave forces. The results of the wave elevation are shown in Figure 3.7. The numerical result deviates from the experimental data for the first three seconds, but the rest of the numerical simulation fits the experiment. The results for the wave force are shown in Figure 3.8. The experimental data vary in the maximum and minimum force in short periodic periods. The numerical result has some minor deviations in the maximum and minimum force between 24 and 30 seconds compared to the experimental data. The numerical model obtained by REEF3D::CFD matches the experimental data well despite the small deviation, and the NWT is validated for wave forces.

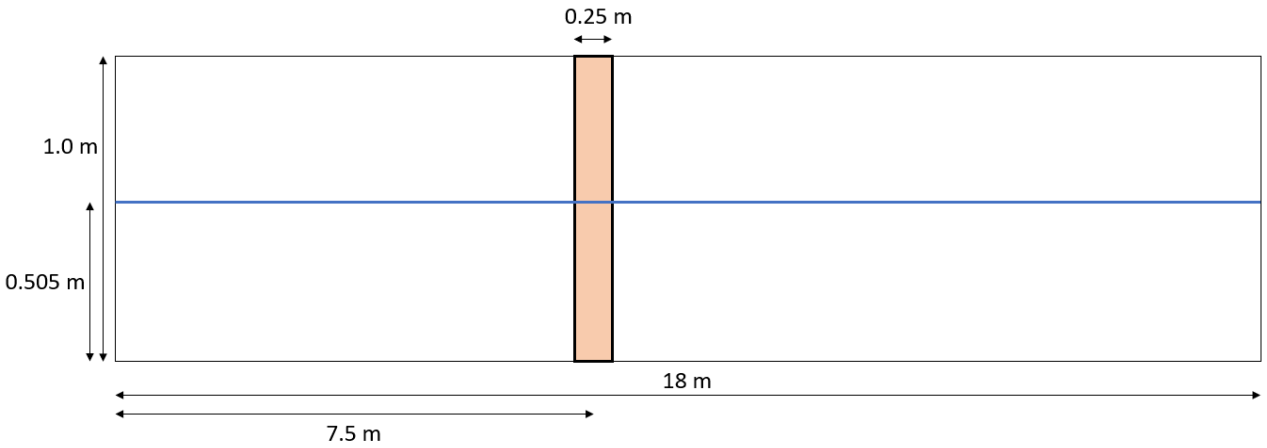

Figure 3.6: Numerical setup for the experiment is obtained from Chen et al. [2014].

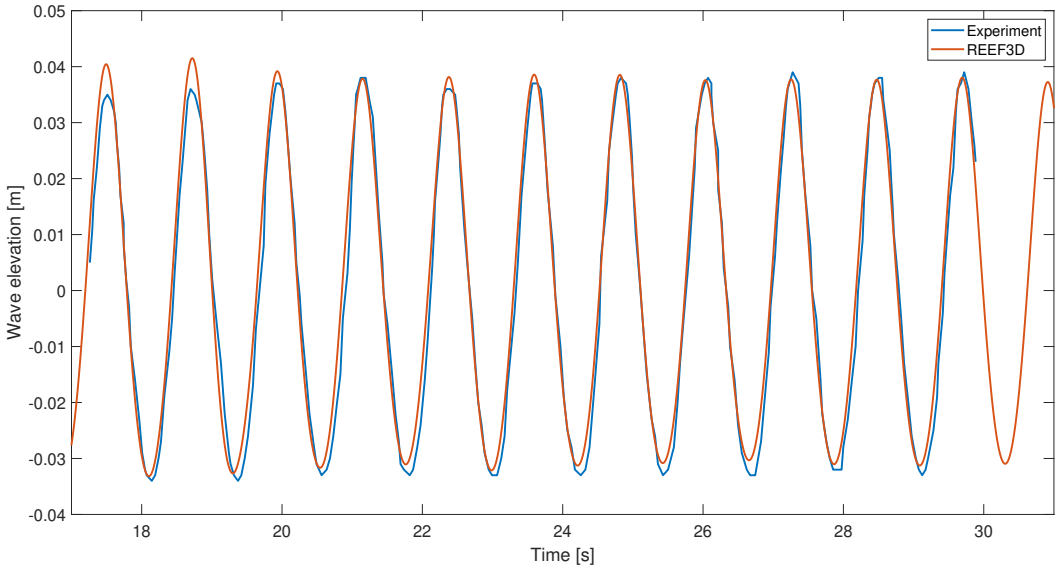

Figure 3.7: Water surface from REEF3D compared to experimental data from Chen et al. [2014]

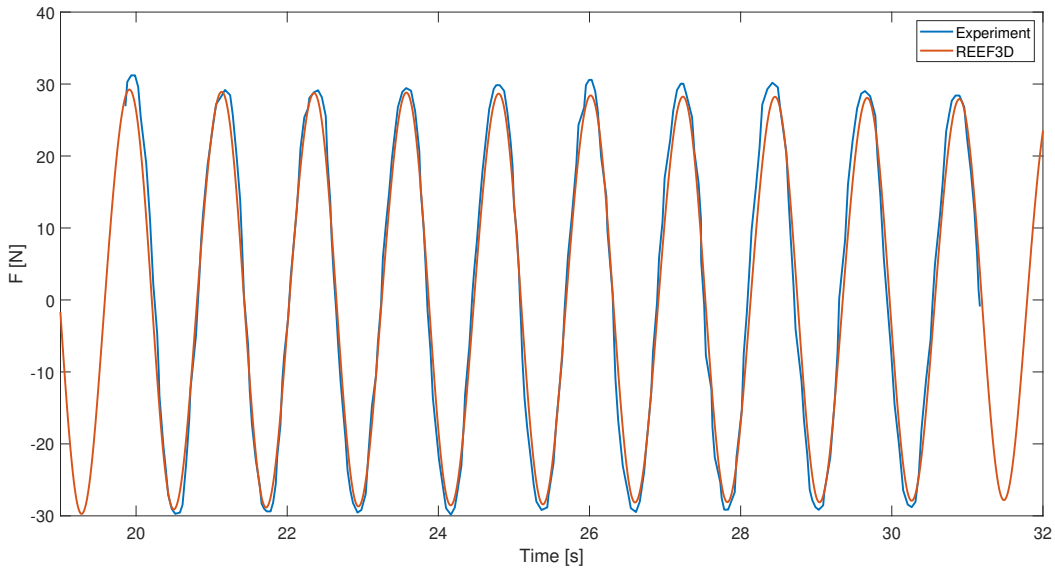

Figure 3.8: Wave forces calculated from REEF3D compared to experimental data from Chen et al. [2014]

Chapter 4

Marine scour

Marine scour is a problem for many offshore structures. Scour affects the integrity of the structures and represents a risk of stability failure. The size of the scour is often measured with scour depth. The value of the scour represents how deeply sediments erode around the structure. Scour depth is an important value in a stability valuation. In the worst case the foundation will fail, but more likely stiffness sensitive structures like wind turbines will be affected due to the change in resistance of the ground. Scour protection is needed in cases with stability problems due to scour. The main goal of this thesis is to investigate a cost-effective and time-effective method to capture the need for scour protection using numerical modelling. Marine scour is a consequence of the interaction between the structure and the flow field of currents and waves. The interaction creates a complex flow field which results in erosion around the structure. REEF3D::CFD can capture the flow field with RANS equations and can describe the scour depth by using a sediment transport model. Scour around a vertical cylinder is considered in this thesis, which is a relevant case for many offshore structures such as platform legs, bridge piers and monopiles.

4.1 Marine scour around a cylinder under current

The numerical results obtained from REEF3D::CFD are compared with the experimental data from Link [2006]. The experiment was carried out in the hydraulic laboratory of the Technical University of Darmstadt. The experiment was built in a rectangular flume that was 37 m long, 2 m wide and 1 m deep. The side walls and the cylinder were made of plexiglass and placed 16 m from the inflow. The diameter of the cylinder was 0.2 m. The flume was filled with a 0.3 m thick layer of sediment. The bed material consisted of natural sand with a d_{50} of 0.00097 m, a density of 2650 kg/m^3, and an angle of repose equal to 29° in air. The present study will examine the experiment with a discharge of 0.18 m^3/s and a water level of 0.3 m. The duration

of the run was 21 h (75.600 s). The numerical model setup for the pier scour case is adopted from Ahmad et al. [2015], as shown in Figure 4.1.

A reduced-length NWT is used for the numerical model. The numerical setup for the flume has a length of 5.5 m, width of 2 m, height of 0.8 m and water depth of 0.3 m. The cylinder is placed in the middle of the flume with a distance of 2.5 m from the inflow. The diameter of the cylinder is 0.2 m. The sediment layer is 0.3 m deep. The selected mesh size is $dx = 0.025$ m. The experimental data contain results as development of the scour over time and contour plot of the scour obtained around the cylinder. The contour plot around the cylinder is shown in Figure 4.2. The sediments are evenly eroded in front of the cylinder with a scour depth reached from 0 to 15 cm. The maximum depth of scour is 15 cm in front of the cylinder. The lee side of the cylinder has a scour depth of 7 cm which decreases to 0 cm in a distance of 25 cm from the backside of the cylinder.

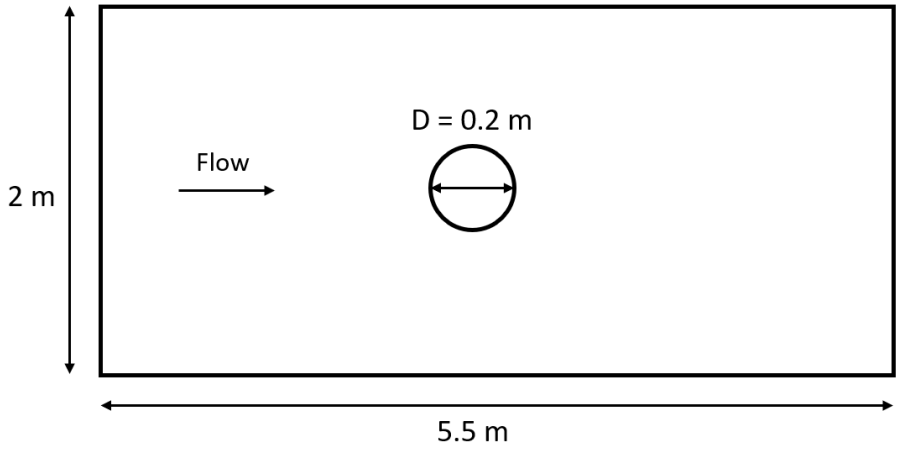

Figure 4.1: Numerical setup for vertical cylinder under current

The numerical results are solved with RANS equations, the level-set method, and the sediment transport model. The scour depth is very sensitive to small changes in the flow field and the sediment transport model, and the model must be accurate to get a good result compared to the experimental data. The sediment transport is described with the bed load transport and the suspended load. The bed load transport for currents is solved with the approach from Engelund and Fredsøe [1976]. This thesis will do a parameter study of the sediment transport model analysis. The parameter study contains investigation of:

- Bed shear stress formulation
- Critical Shields parameter, θ_c

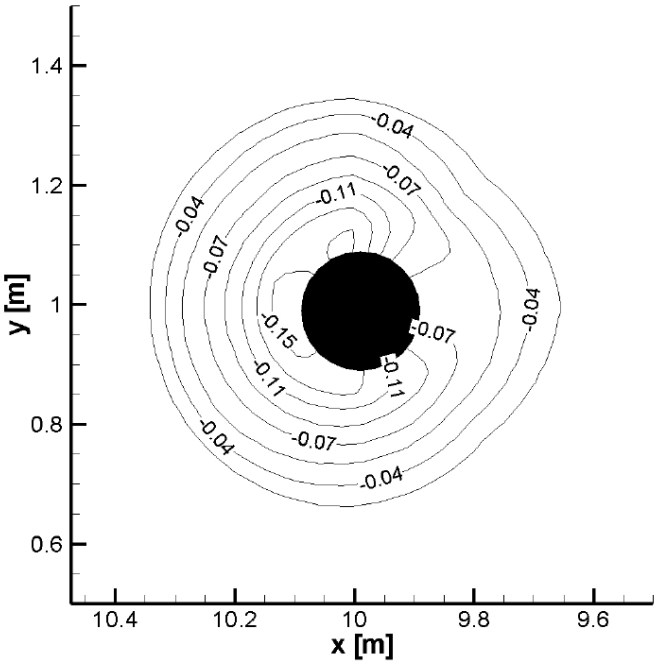

Figure 4.2: Contour of the scour at the end of the experiment from Link [2006], figure obtained from Bihs [2011]

- Shear stress reduction
- Sandslide algorithm
- Equivalent sand roughness, k_s
- Suspended transport load

4.1.1 Bed shear stress formulation

The approach from Engelund and Fredsøe [1976] calculates bed load transport using the bed shear stress and the critical bed shear stress. The bed shear stress is calculated with formulations based on wall function/velocity, friction coefficient/velocity, velocity, or turbulent kinetic energy. The calculated bed shear stress is illustrated in Figure 4.3.

The bed shear stress has a huge influence in the bed load transport. The bed shear stress formulations are expected to calculate bed shear stresses that give a development of the scour depth similar to the experimental data. Different formulations are based on different assumptions, but it is expected that they will determine almost the same bed shear stress. Figure 4.3 (c) shows a significant difference in bed shear stress

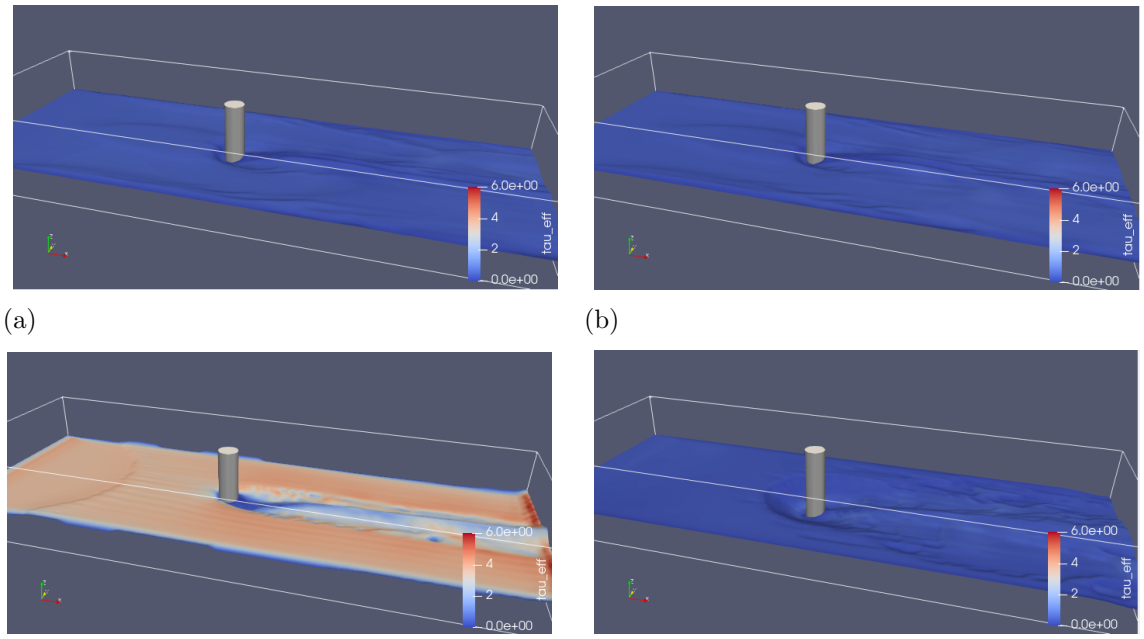

Figure 4.3: Bed shear stress based on (a) wall function/velocity, (b) friction coefficient/velocity, (c) velocity and (d) turbulent kinetic energy. The blue color represents zero bed stress and the red color represents 6 kPa as bed shear stress.

compared to (a), (b) and (d). The bed shear stress is expressed with a color range from blue to red. Blue represents 0 kPa and red represents 6 kPa. The bed shear stress formulation based on (c) velocity calculated about 4 kPa as the maximum bed shear stress. The bed shear stress formulation based on (a) wall function/velocity, (b) friction coefficient/velocity and (d) turbulent kinetic energy calculated about 0.5 kPa as maximum bed shear stress. The difference in bed shear stress is almost 3.5 kPa and the shear stress based on velocity is about 8 times greater. The difference in bed shear stress gives the development in scour depth as shown in Figure 4.4. The consequence of zero bed shear stress is no sediment erosion. The bed shear stress must be higher than the critical shear stress to initiate motion of sediments. The critical shear stress is calculated with the Shields parameter given in Shields [1936]. Shields parameter in Figure 4.4 is $\theta_c = 0.047$. Shields parameter is a non-dimensional number used to calculate the initiation of motion in sediments. The initiation of motion begins when the bed shear stress is greater than the critical bed shear stress. The critical bed shear stress does not depend on the chosen bed shear stress formulation, which is the main reason for zero scour for three of the bed shear stress formulations shown in Figure 4.4.

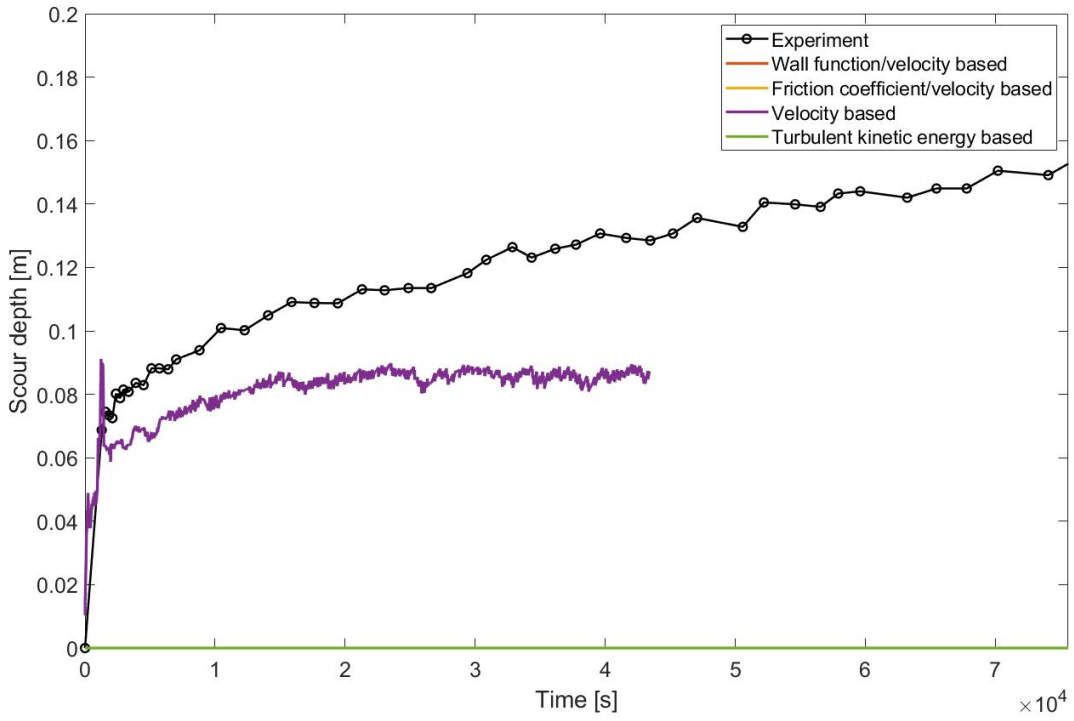

Figure 4.4: Development of scour depth with $\theta_c = 0.047$ is shown for bed shear stress formulation based on wall function/velocity, friction coefficient/velocity, velocity and turbulent kinetic energy.

The scour development is impossible to interpret for the simulations with bed shear stress calculated based on wall function/velocity, friction coefficient/velocity and turbulent kinetic energy since the motion of the sediment is never initiated. The critical shear stress must be reduced to investigate the development of the scour depth. Critical Shields parameter is reduced to $\theta_c = 0.01$ in Figure 4.5. The result for the formulation of the bed shear stress wall function/velocity and the friction coefficient/velocity is almost similar. The scour depth reaches a depth of 0.11 m while the experimental data never converge but reach 0.15 m after 21 hours. The result of the bed shear stress formulation based on turbulent kinetic energy is illustrated with the purple line in Figure 4.5. The scour depth from the numerical simulation ends 0.1 m higher than in the experiment. The depth of scour never converges, which is similar to the experimental data.

The contour plot of the scour formation from the experimental data is shown in Figure 4.2 compared to the results of REEF3D presented in Figure 4.3. The contour plot from the experimental data shows a circular formed hole with a lesser scour depth on the lee side of the cylinder. The result from the bed shear stress formulations based

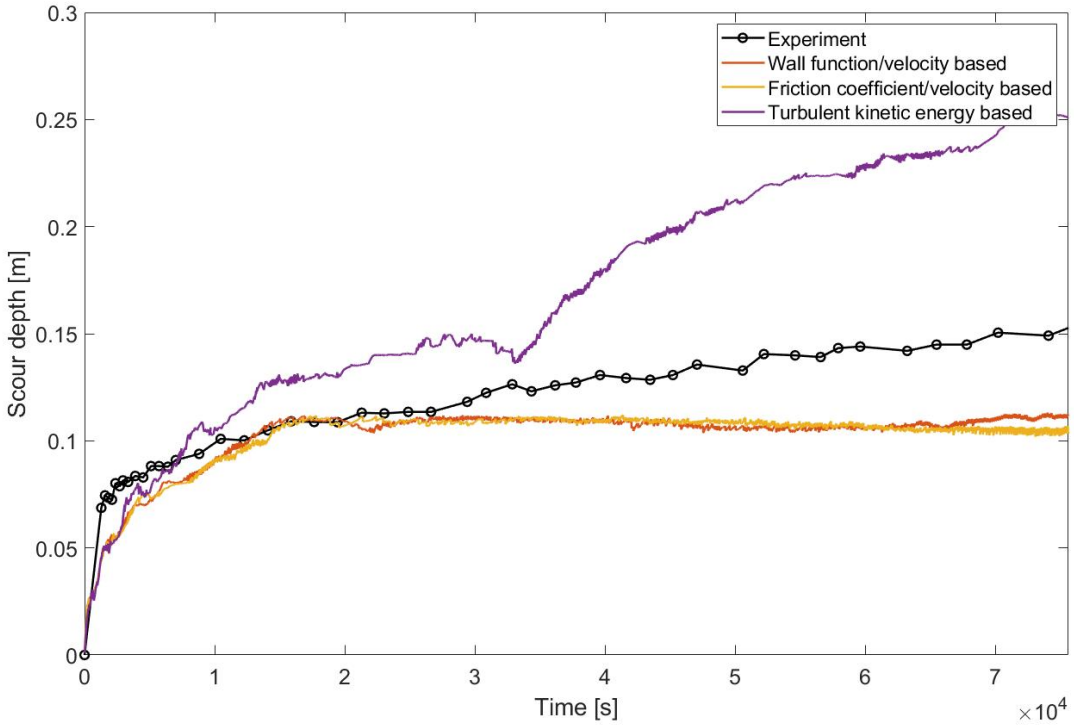

Figure 4.5: Development of scour depth is shown for bed shear stress formulation based on wall function/velocity, friction coefficient/velocity and turbulent kinetic energy.

on wall function/velocity, friction coefficient/velocity and velocity show a scour hole that deviates from the experiment. The experiment has maximum scour in front of the cylinder, but the results from REEF3D show maximum scour on the sides of the cylinder. The scour hole for the simulation based on turbulent kinetic energy is more similar to the contour plot from the experiment. The shape is circular with maximum scour in front of the cylinder. The erosion around the cylinder shows a smooth circular shape similar to the experimental data. The diameter of the scour hole is larger than the scour hole in the experiment, but that can be a consequence of the higher maximum scour depth.

4.1.2 Shear stress reduction

The shield parameter has a huge impact on the critical shear stress. Critical Shields parameter does not take the sloping bed into account, and a reduction factor is introduced for the sloping bed. The reduction factor can be calculated from several approaches that affect critical shear stress. Figure 4.6 shows the resulting development

of scour depth with the reduction factor from Fredsoe and Deigaard [1992] and Kovacs and Parker [1994]. The results converge against a scour depth of 0.085 m which is considerably lower than the scour depth in the experiment. The reduction factor calculated with Kovacs and Parker [1994] shows a slightly higher scour depth than the result calculated with Fredsoe and Deigaard [1992]. Kovacs and Parker [1994] calculates a scour depth that is easier to read since the graph is less varied. The reduction factor from Fredsoe and Deigaard [1992] shows a result that is more variable which can be an indication of numerical difficulties.

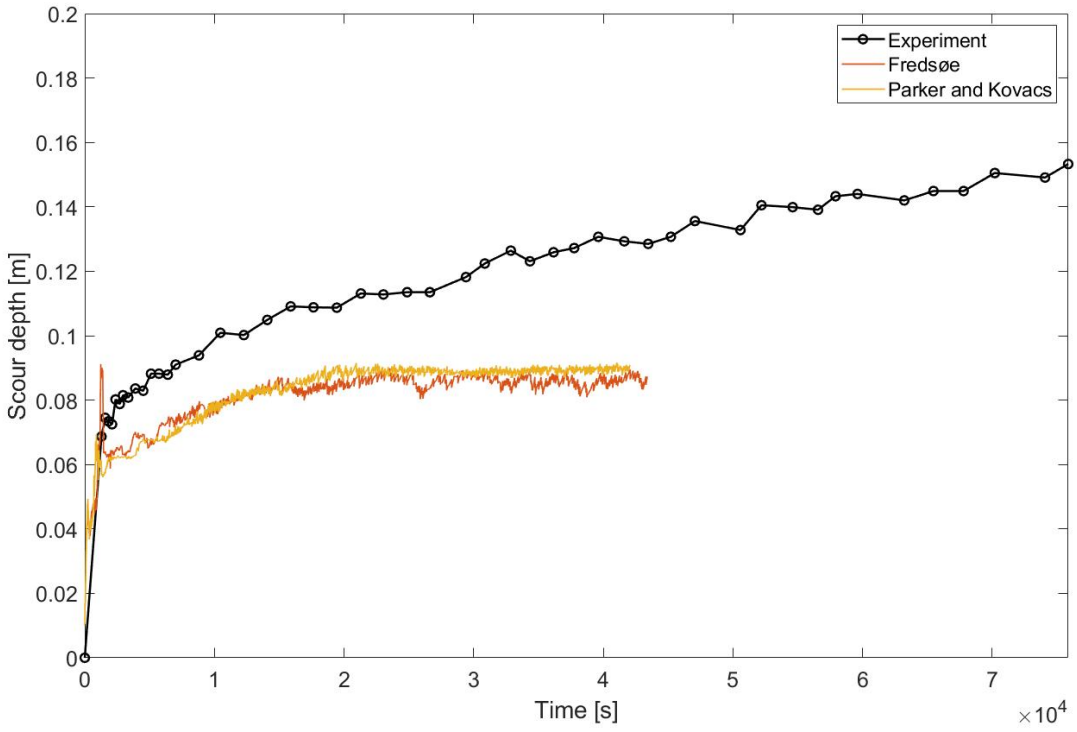

Figure 4.6: The scour depth over time is shown for bed shear stress reduction factor calculated with Fredsøe (red line) and Kovacs and Parker (yellow line).

Figure 4.7 shows the topography for the bed surface. The topography is very similar to each other, but the topography is smoother in (b). The development of scour depth also shows a smoother development for (b) rather than (a). The simulation with reduction factor from Fredsoe and Deigaard [1992] has a rougher development of scour depth and the topography, which indicates some minor difficulties in capturing the exact scour depth. Despite the small differences, the results of both reduction factors are almost similar.

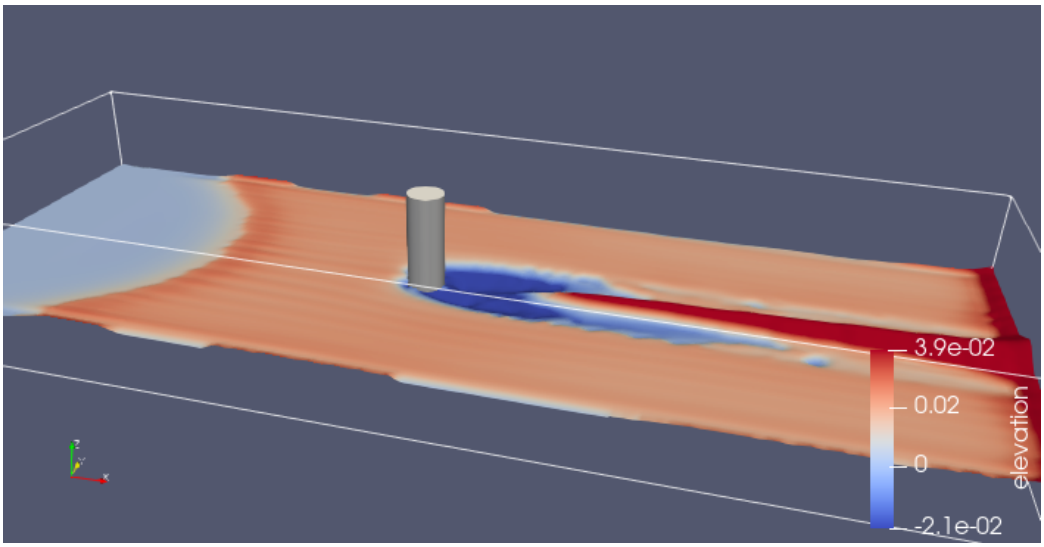

(a)

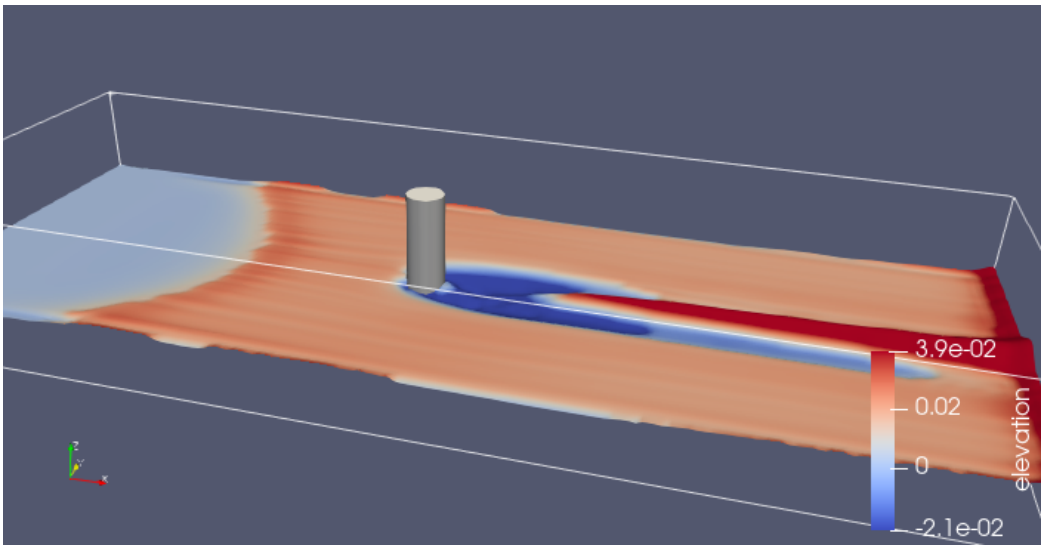

(b)

Figure 4.7: The topography of the bed surface in the NWT is colored with elevation from -0.021 m in blue to 0.039 m in red. Figure (a) is simulated with the reduction factor by Fredsoe and Deigaard [1992] and (b) is calculated with reduction factor from Kovacs and Parker [1994].

4.1.3 Sandslide algorithm

Sandslide algorithms are an important model for calculating the size of the scour hole. The effect of using different sandslide algorithms is shown in Figure 4.8. The difference between Burkow [2010] and Wu [2007] is huge. The yellow line describes the development of the scour calculated with the Wu sandslide model, and the red line describes the Burkow sandslide model. The yellow line increases fast and the simulation stops due to irregular values. The red line shows the result of a simulation without irregular values. Even if the simulation works, the reached scour depth is lower than the values from the experiment. The simulation with sandslide algorithm from Wu is tested with a lower critical Shields parameter and a different formulation for bed shear stress to run the simulation without irregular values. This simulation is shown with the purple line in Figure 4.8. The purple and red lines follow each other and almost reach the same scour depth at the end.

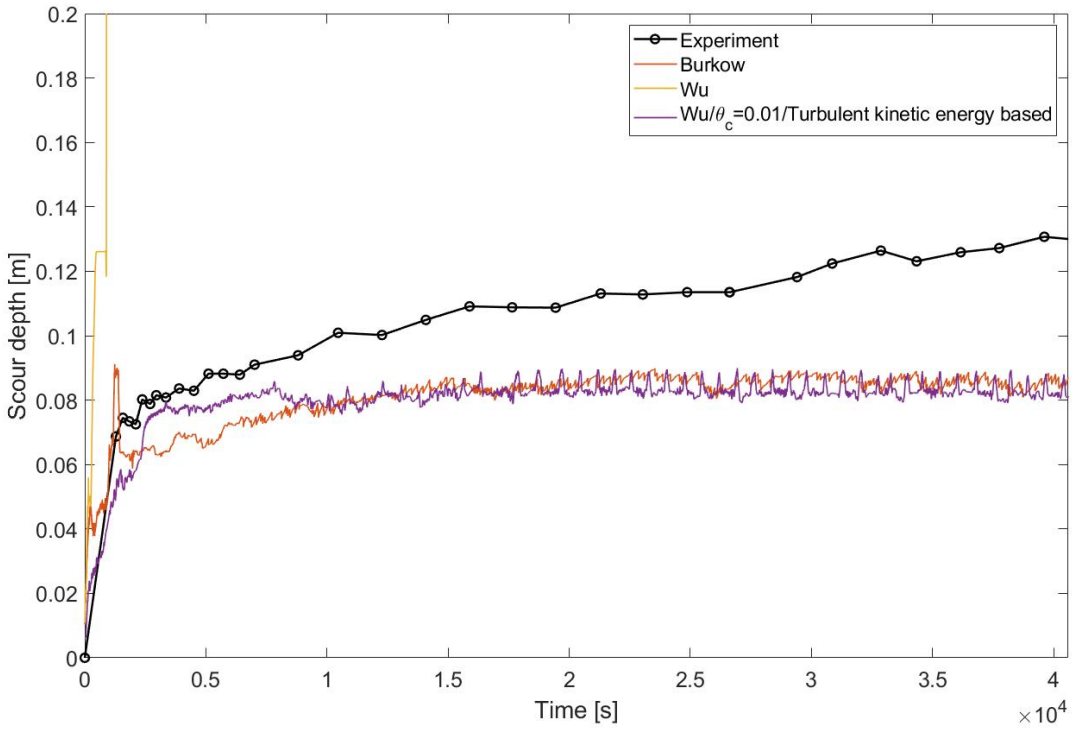

Figure 4.8: The sandslide algorithm is calculated with Burkow [2010] and Wu [2007]. The simulation with Wu is also done in combination with $\theta_c = 0.01$ and bed shear stress based on turbulent kinetic energy.

Figure 4.9 shows the topography of the sediment layer. The simulation modeled with Burkow [2010] shows scour concentrated in a straight line on the backside of the

cylinder. Figure 4.9 (b) shows a scour pattern where the erosion is occurring over the full width. The contours of the sediment layer around the cylinder vary greatly due to erosion on the sides and zero change in bed level in front and back of the cylinder. The result calculated with the Wu sandlide model deviates from the contour plot from the experiment shown in Figure 4.2.

Initiation of motion requires higher bed shear stresses than the critical shear stress. Figure 4.10 (a) show the bed shear stress illustrated in Paraview after 75000 seconds. The maximum bed shear stress is 0.68 kPa located in the scour hole, and the critical shear stress must be less than 0.68 kPa to initiate sediment motion. Figures 4.10 (b) show the critical shear stress illustrated in Paraview after 75000 seconds. The maximum critical shear stress is about 0.2 kPa located in the scour hole. The bed shear stress is higher than the critical shear stress which results in bed load transport. The consequence of bed load transport are increasing scour depth unless the sandslide algorithm redistribute the sediments into the scour hole due to steep sides. The development of scour for the simulation in Figure 4.10 are shown in Figure 4.4. The development of scour is still increasing after 75000 seconds, which means the bed load transport erode sediments without the sandslide algorithm redistribute sediment back into the scour hole.

Figure 4.11 shows the bed shear stress and the critical shear stress. The bed shear stress is higher than the critical shear stress and bed load transport will occur. The development of scour depth shown with the purple line in Figure 4.8 converge against 0.8 m scour depth. The bed load transport erode sediments in the scour hole until the sandslide algorithm get triggered and fill the hole with sediments again. The scour depth find an equilibrium between bed load transport and the sandslide algorithm which end up with scour depth of 0.8 m.

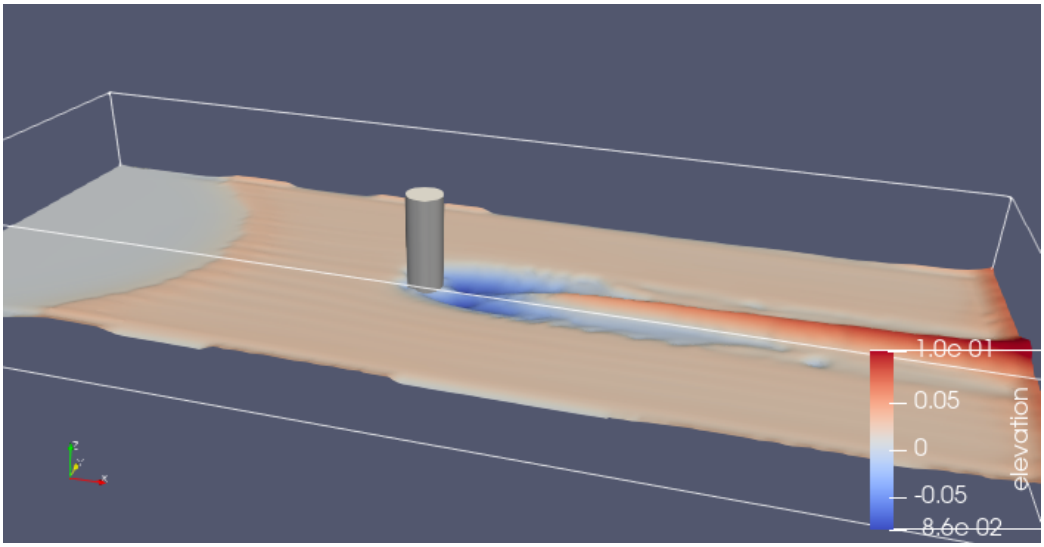

(a)

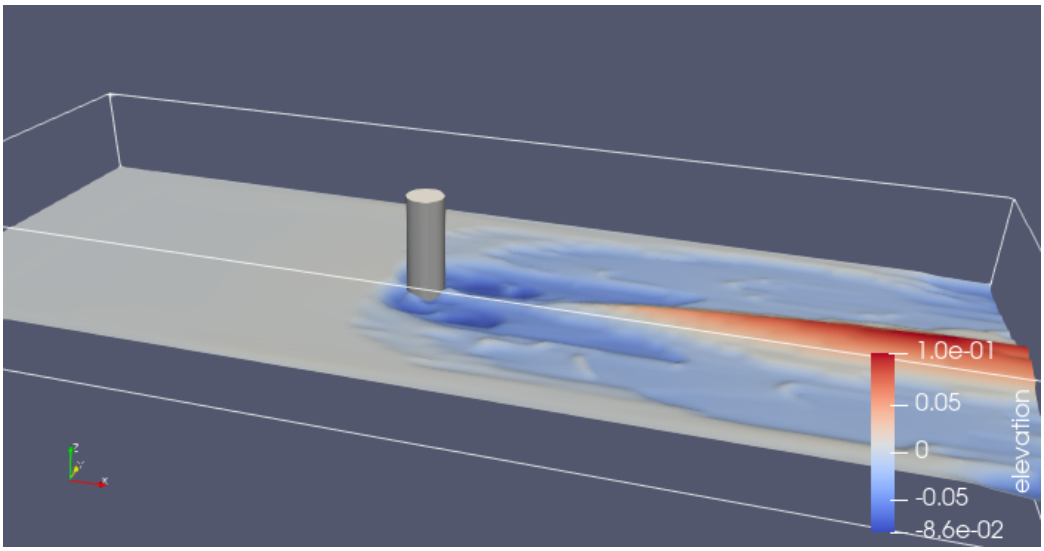

(b)

Figure 4.9: The topography of the bed surface in the NWT is colored with elevation from -0.086 m in blue to 0.1 m in red. Figure (a) is simulated with the sandslide algorithm from Burkow [2010] and (b) is calculated with the sandslide algorithm from Wu [2007] combined with $\theta_c = 0.01$ and bed shear stress based on turbulent kinetic energy.

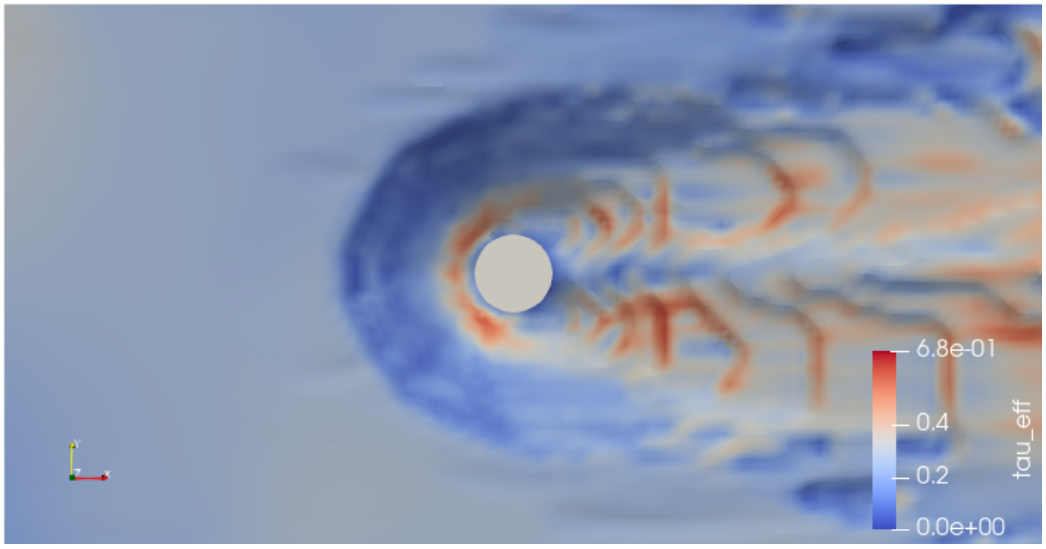

(a)

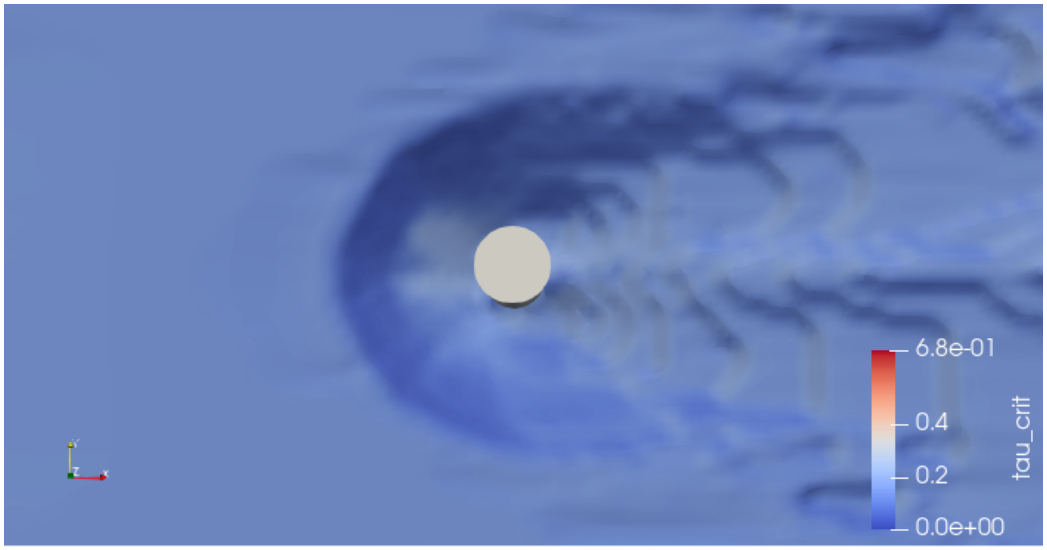

(b)

Figure 4.10: The bed shear stress is given in (a) and the critical shear stress is shown in (b).The sandslide algorithm from Burkow [2010] in combination with $\theta_c = 0.01$ and bed shear stress based on turbulent kinetic energy.

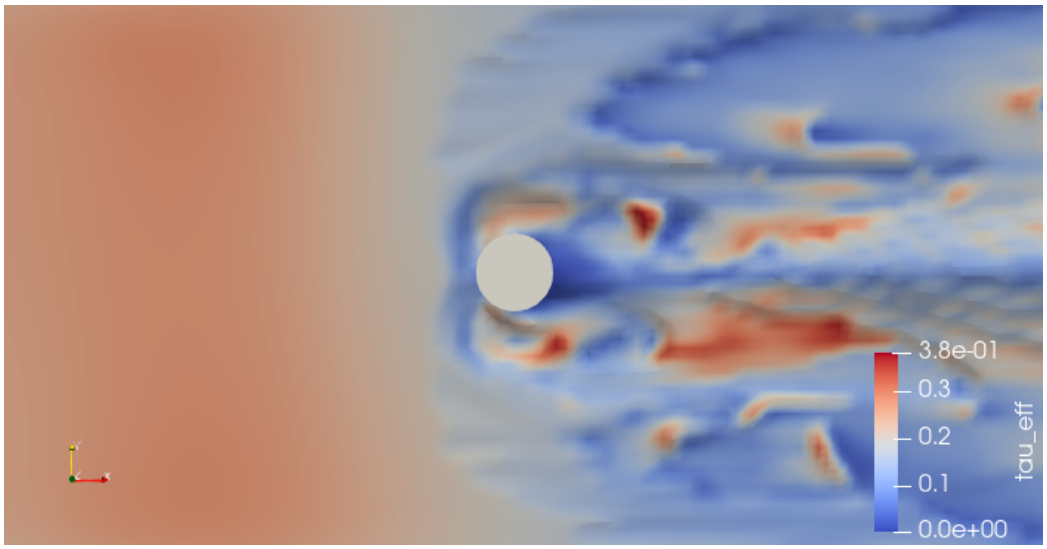

(a)

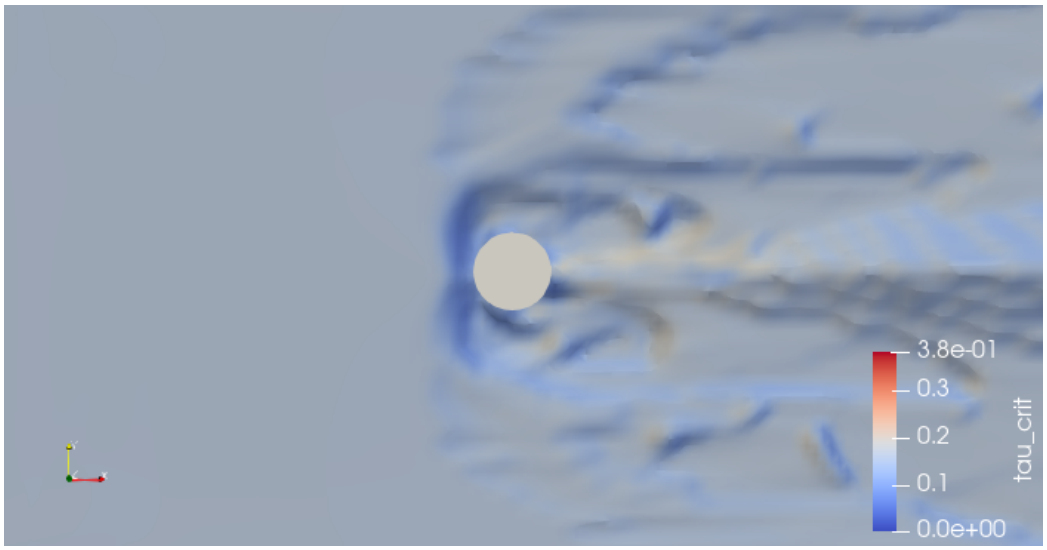

(b)

Figure 4.11: The bed shear stress is given in (a) and the critical shear stress is shown in (b). The sandslide algorithm is calculated with Wu [2007] in combination with $\theta_c = 0.01$ and bed shear stress based on turbulent kinetic energy.

4.1.4 Equivalent sand roughness, k_s

The bed shear stress is also depended on the material properties of the sediment. The equivalent sand roughness is investigated and the result is shown in Figure 4.12. The sand roughness is used in Eq. 1.1 where higher sand roughness will result in a higher shear velocity. A higher calculated shear velocity is expected to result in a deeper scour depth in the numerical wave tank. Figure 4.12 presents the development of scour depth using different factor for d_{50} in the calculation of sand roughness, k_s. The model is simulated with the factor for d_{50} equal to 3 and 5. The yellow line reaches a higher scour depth than the red line, and the yellow line represents the simulation with the highest sand roughness. Figure 4.12 demonstrates that higher sand roughness results in higher scour depth.

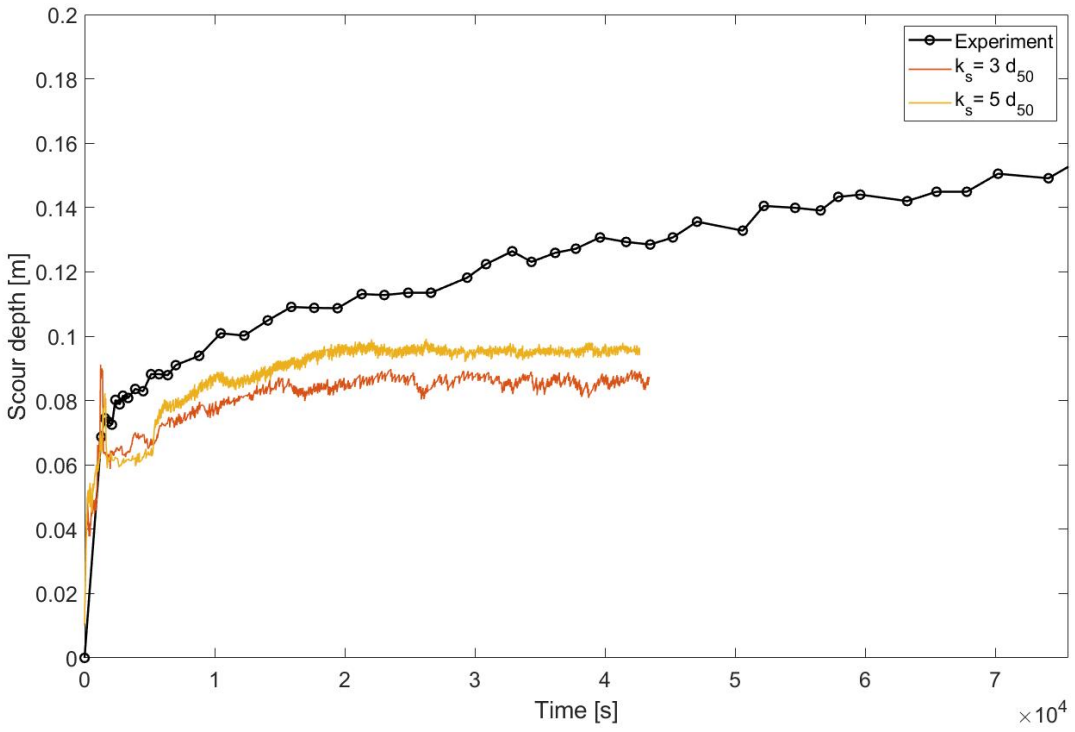

Figure 4.12: Development of scour depth over time for simulations with factor for d_{50} equal to 3 (red) and 5 (yellow).

4.1.5 Suspended transport load

Total sediment transport contains both bed load transport and suspended load transport. Suspended load transport represents all sediments that are lifted from the surface of the bed, where the sediments are transported without continuous contact with the bed. Suspended load transport appears when the bed shear stress is much higher than the critical shear stress. Suspended load transport is tested for several numerical setups. The effect of adding suspended load is investigated in Figure 4.13. The numerical setup in Figure 4.13 (a) has $\theta_c = 0.047$ and bed shear stress based on velocity. Numerical setup in Figure 4.13 (b) has $\theta_c = 0.01$ and bed shear stress based on turbulent kinetic energy. The numerical setup for Figure 4.13 (c) has $\theta_c = 0.01$ and has a bed shear stress based on friction coefficient/velocity. Figure 4.13 (a) shows the result with suspended load in yellow and without suspended load in red color. The simulation with suspended load has some problems with the numerical model due to the unlikely development of the scour depth. The scour depth deviates from the experimental data and the simulation without suspended load. The results show that the simulation is more exposed to numerical faults with the use of suspended load.

The suspended load transport is still important to investigate and is considered with another numerical setup in Figure 4.13 (b). The yellow line represents the simulation with suspended load transport and the red line without. The scour depth development follows each other for the first 10,000 seconds of the simulation. The red line continues to rise until the end of the simulation. The yellow line converges after 25000 seconds of the simulation. The result shows that the suspended load contributes to refill the scour hole with sediments rather than digging the scour hole deeper. The assumption is made since the simulation without suspended load transport is higher. The yellow line becomes flat and has no variations after the simulation has runned for 25000 seconds. The flat curve can be a consequence of a numerical fault. Figure 4.13 (a) and (b) show that the numerical model is more exposed to numerical faults and the suspended load contributes to the filling of the scour hole. The result was investigated with the last numerical setup in Figure 4.13 (c). The yellow line shows the development of scour depth with suspended load transport and the red line without suspended load. The result confirms that the suspended load contributes to the refill of the scour hole, as the scour depth reaches a lower scour depth with the use of the suspended load. The result does not indicate any numerical fault which is different from the other simulation. The investigation of suspended load transport shows an important impact of the development of scour depth.

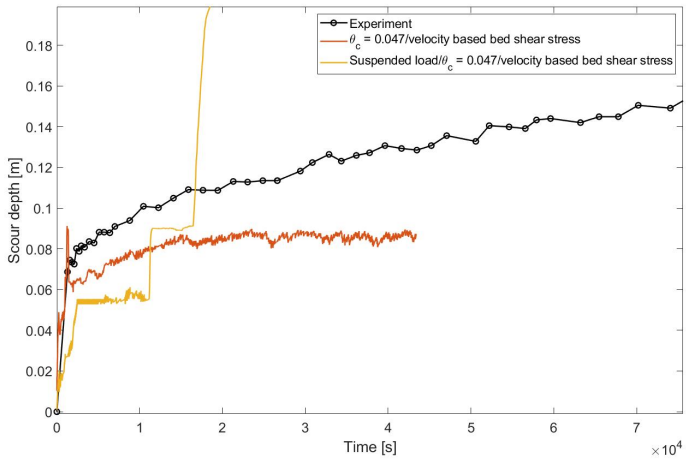

(a)

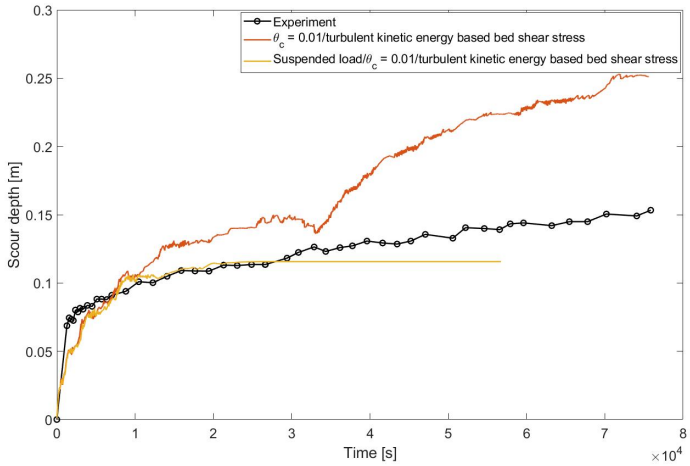

(b)

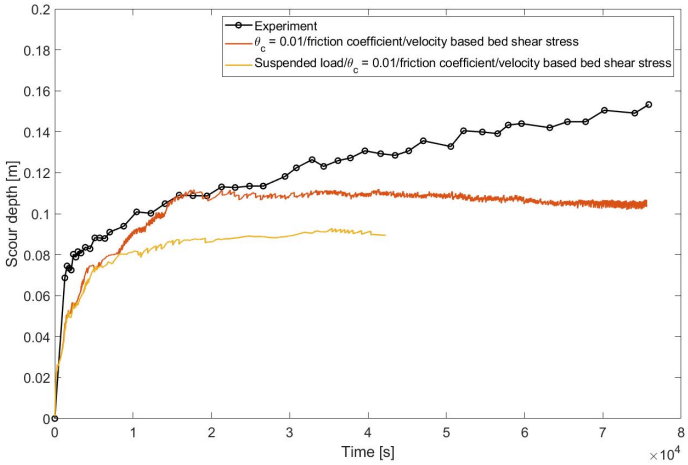

(c)

Figure 4.13: Compared development of scour depth over time with and without suspended load transport for simulations with different numerical setup.

4.2 Marin scour around a cylinder with different diameter

The results of the simulation in Section 4.1 have difficulties in calculating a numerically good fit to the experimental data. The numerical model is calculated by creating a mesh. The mesh is important for capture of the flow field, and small cylinders can make it difficult to capture an accurate flow field. The effect of the change in diameter is investigated and the results are given in Figure 4.14.

The numerical model is tested with cylinders with diameters equal to 0.2 m, 0.4 m, 0.6 m, 0.8 m and 1.0 m. The numerical model in section 4.1 contains a cylinder diameter equal to 0.2 m. The scour around the cylinder will change due to a change in the flow field. The flow field is expected to capture higher velocities since a bigger cylinder will change the flow field over a larger area and it is expected that the velocities will rise around the cylinder. The velocities are expected to increase with larger diameter since the distance around the cylinder becomes longer. The consequence of higher velocities is a deeper scour depth.

The mesh size is important for the flow field and interaction between the structure and the water. The flow field around the cylinder could be captured better with more elements surrounding the cylinder. More elements could produce more accurate results due to a better covering of the cylinder.

The development of the scour is represented with scour depth over time in Figure 4.14. The result for a diameter equal to 0.2 m converges towards a scour depth of 0.1 m. The result for a diameter equal to 1.0 m rises to a scour depth of 0.32 m. The NWT is filled with 0.3 m of sand, which means that the sand is eroded to the bottom of the NWT. This means that a larger diameter results in a larger scour depth. The simulations for diameters in between show a clear trend that larger and larger diameters give greater and greater scour depth.
The topography of the sand surface is given in Figure 4.15. The topography does not seem to change significantly, other than that all formations enlarge. The scour hole becomes larger, but the shape of the hole looks the same. The result does not indicate that a larger diameter results in a more accurate and stable response.

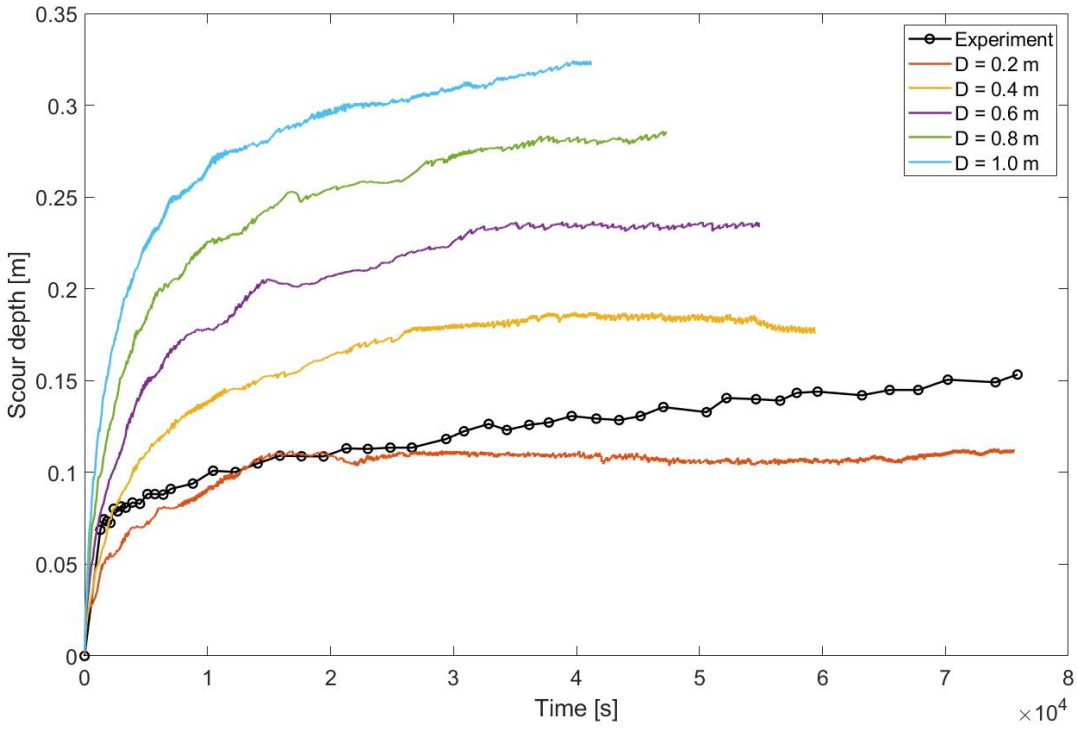

Figure 4.14: The development of scour depth for the numerical model with different diameters, D. The numerical setup has bed shear stress formulation based on wall function/velocity and $\theta_c = 0.01$.

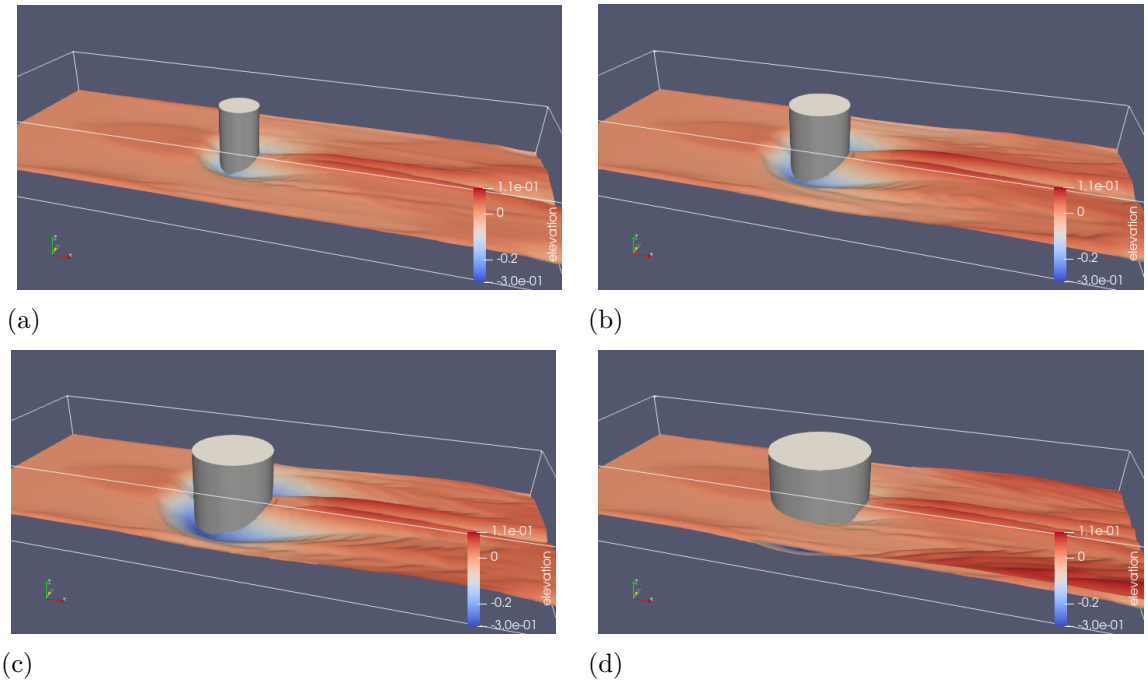

(a) (b)

(c) (d)

Figure 4.15: Topography at bed level. The numerical setup contain bed shear stress based on wall function/velocity and $\theta_c = 0.01$. The numerical models have a diameter equal to $D = 0.4$ (a), $D = 0.6$ (b), $D = 0.8$ (c) and $D = 1.0$ (d).

Chapter 5

Scour protection

The main purpose of scour protection is to reduce the scour depth. There are several types of scour protection, but good scour protection will reduce scour, be cost-effective, and predictable. Traditional scour protection of rocks involves building an extra layer with rocks on top of the sea bottom. A filter layer is needed below the rock layer. The filter and the rock layer are combined into one layer in some designs. Traditional scour protection of rocks has been shown to work in currents, but has problems in waves. The scour protection in wave-dominated areas is preferable to have a low profile.

Gabions are an alternative method. The method is very similar to the traditional scour protection of rocks, but gabions can use smaller stones that implies better filter conditions. Concrete mattresses are another method consisting of concrete bricks attached together with ropes. Concrete mattresses provide low protection against horseshoe vortex, but are effective as cover layer with a filter layer below. Old tires are another method where the scour depth is observed to be reduced. Scour protection with the use of artificial seaweed is also used. The frond reduces the velocities on the seabed, resulting in lower bed shear stresses. Artificial seaweed will accumulate sediment as a result of reduced velocities.

The design of scour protection must consider several risks and challenges. Sumer et al. [1992] assume that there are five failure mechanisms regarding scour protection designs:

- Erosion of the protective layer
- Scour of the layer beneath the protective layer
- Scour at the edges of the scour protection

- Destabilization by bed-form progression
- Sinking of the scour protection due to various factors (liquefaction, scour below the individual stones, etc.)

Arboleda Chavez et al. [2019] investigate traditional scour protection of rocks in a large-scale experiment. This experiment focuses on erosion of the protective layer and edge scour. The experiment was carried out at the HR Wallingford Fast Flow Facility as part of the European HYDRALAB-PLUS PROTEUS (Protection of offshore wind turbine monopiles against scouring) project. The experiment captured damage of the protection by measuring the topography of the scour protection and the sand pit with a laser scanner. The results of one of the tests are shown in Figure 5.1.

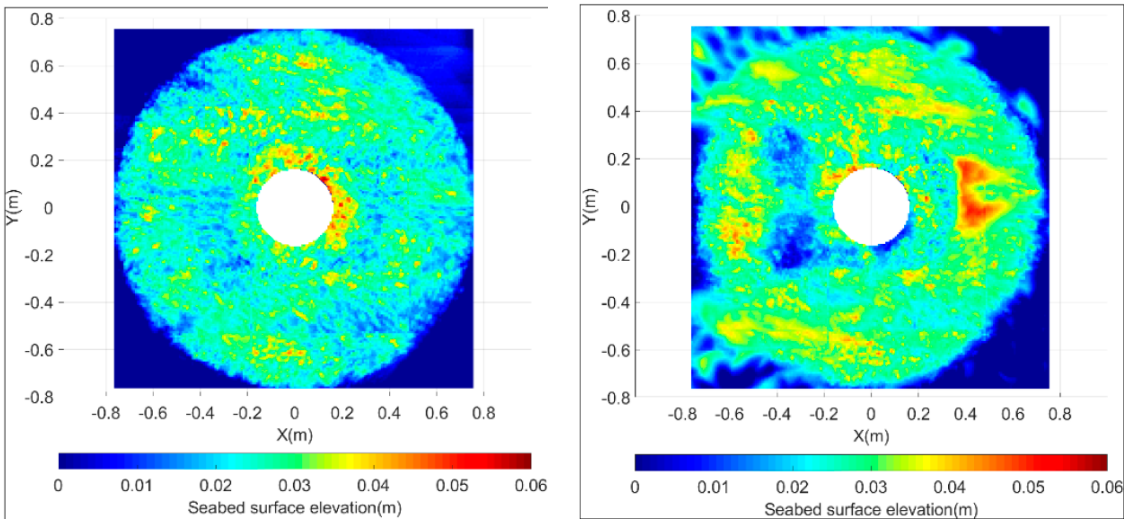

(a) (b)

Figure 5.1: Topography of the scour protection material and of the sand pit measured by the laser scanner before Test 03 (a), and after 3000 waves at the end of Test 04 B (b) in the experiment, figure obtained from Arboleda Chavez et al. [2019].

Most of the scour is centered around the cylinder where the scour protection works as a shield against erosion of the sand pit. Scour of the sand pit are the main erosion that generates stability problems and is therefore protected by the protective layer. The protective layer ensures that the sand pit is not affected by scour. In this experiment, the durability of the scour protection is investigated. This paper will not explore a numerical model for the durability of the protective layer. The sediment model in REEF3D::CFD is based on results from experimental data which are limited to sediments with grain size equal to sand. Scanning protection contains rocks, which means that the sediment model is not valid for the protective layer. The

durability of the protective layer will not be investigated with REEF3D::CFD due to the limitations in the sediment model.

Figure 5.1 shows an almost unaffected sand pit with the use of scour protection. Scour protection gives huge benefits to the stability of the structure. Scour protection is expensive and will only be used if necessary. It is financially more expensive with scour protection with a larger diameter because more sediments are needed. This thesis will look at the effect on scour when the numerical model applies different diameters for the scour protection. The top view of the numerical model is shown in Figure 5.2 and the side view is shown in Figure 5.3.

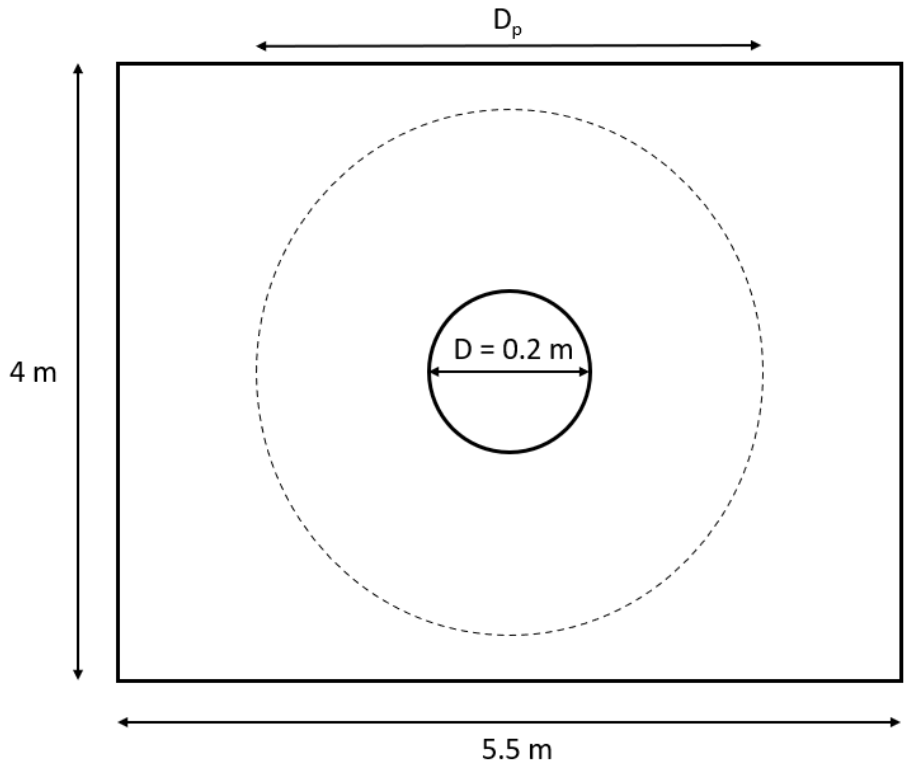

Figure 5.2: Top-view of the numerical model. The cylinder is market as a circle with a solid line and the dotted line represent the diameter of the scour protection.

The protective layer in the numerical model is built with a solid structure instead of sediments, as was done in the experiment. The numerical model will generate edge scour that deviates from the result in the experiment as a consequence of the solid protective layer. The protective layer has no angle of repose and cannot be eroded. The protective layer acts as an additional cylinder with a larger diameter with a height of 0.1 m over the bed surface. The numerical model is tested for one

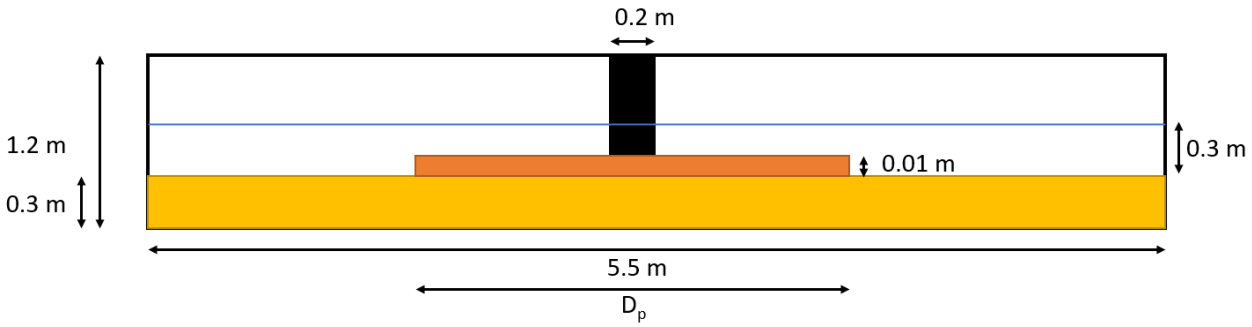

Figure 5.3: Side-view of the numerical model with dimensions.

simulation with bed shear stress based on wall function/velocity and one simulation with bed shear stress based on turbulent kinetic energy.

The development of scour depth for the simulation with bed shear stress based on wall function/velocity is given in Figure 5.4. The result presents the scour depth for numerical models with diameter of the scour protection equal to 0.2 m, 0.4 m, 0.6 m, 0.8 m and 1.0 m. The simulation with $D_P = 0.2$ m converge against 0.11 m, and the simulation with $D_P = 1.0$ m converge against 0.045 m. The results show that the protection of the scour with a larger diameter converges against a lower depth of the scour.

Figure 5.4 shows that the effect of scour protection decreases after reaching a certain diameter. It is therefore appropriate to use a diameter that secures the cylinder from scour, but is also financially beneficial. The effect of increasing the diameter decreases drastically for diameters larger than 0.6 m.

It is also important to take into account the topography of the simulations. The numerical model has weaknesses in relation to the experimental model that result in some other result. The topography of this simulation is shown in Figure 5.5. The figure shows how the sediments from the sand pit erode and deposit around the cylinder. The maximum scour is located along the back of the scour protection. This edge scour would have been more even if the protective layer consisted of rocks. The result does not give a realistic picture of what the topography at the bottom would be like, but the assumption that scour protection gives a positive effect on scour depth is reasonable.

The development of scour varies between the different numerical setups. The scour protection are therefore tested in another numerical setup. Figures 5.6 and 5.7 have the bed shear stress formulation based on turbulent kinetic energy and $\theta_c = 0.01$. The

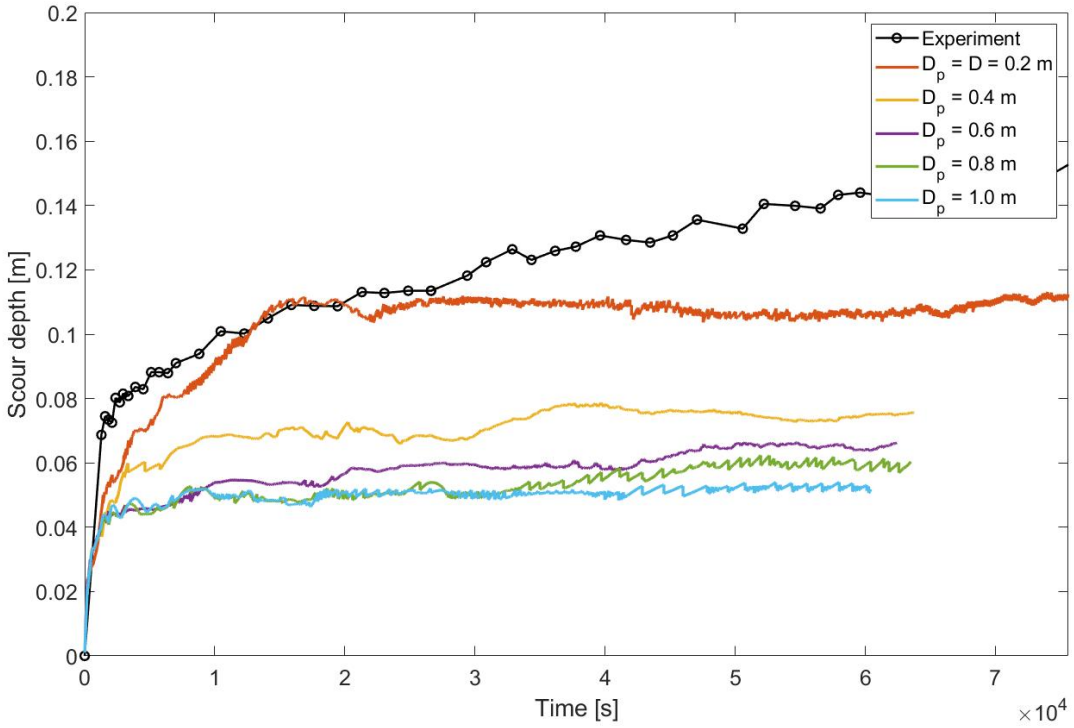

Figure 5.4: Development of scour depth in sand pit with scour protection with different diameters, D_P. The numerical setup contain bed shear stress formulation based on wall function/velocity and $\theta_c = 0.01$.

results verify the result from the other numerical setup and show that the protection of the scour with a larger diameter converges against a lower depth of the scour.

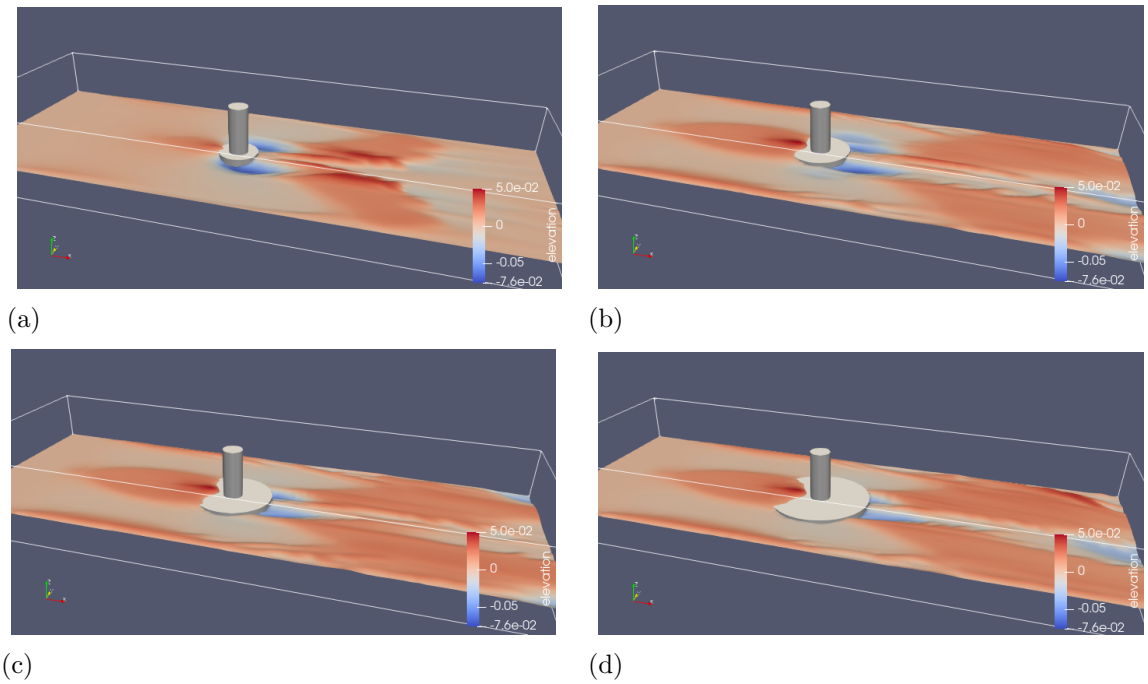

Figure 5.5: Topography of the surface of the bed. The numerical setup contains the bed shear stress based on the wall function / velocity and $\theta_c = 0.01$. The scour protection has a diameter equal to $D_P = 0.4$ in (a), $D_P = 0.6$ in (b), $D_P = 0.8$ in (c) and $D_P = 1.0$ in (d).

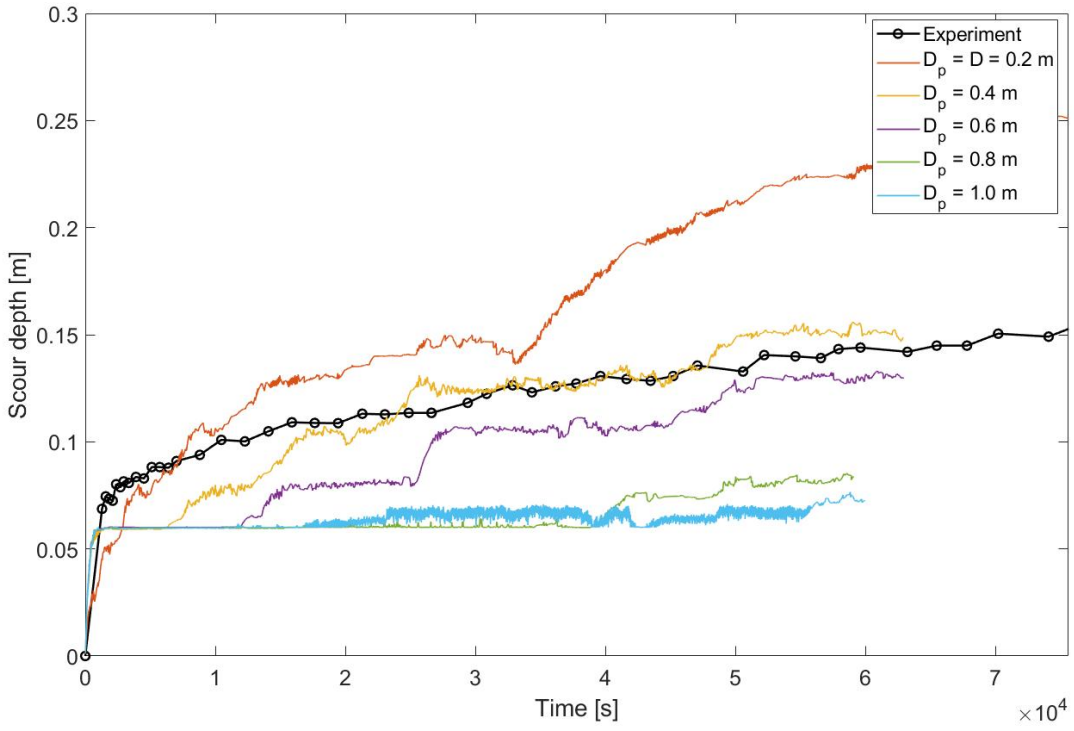

Figure 5.6: Development of scour depth in sand pit with scour protection with different diameters, D_P. The numerical setup contain bed shear stress formulation based on turbulent kinetic energy and $\theta_c = 0.01$.

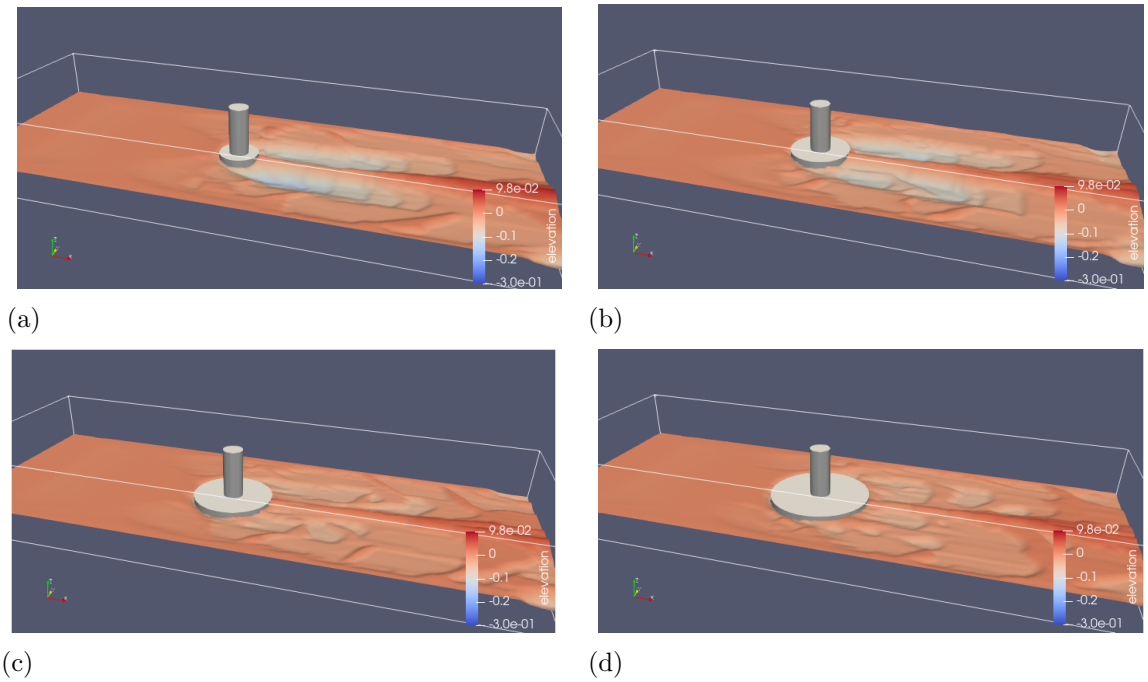

(a) (b)

(c) (d)

Figure 5.7: Topography of the surface of the bed. The numerical setup contains bed shear stress based on turbulent kinetic energy and $\theta_c = 0.01$.

Chapter 6

Conclusions and suggestions for further work

6.1 Summary

This thesis has investigated many parameters in the sediment transport model calculated by REEF3D::CFD. This parameter study was examined for scour around a cylinder under current. The investigations look into parameters such as bed shear stress formulation, critical Shields parameter, shear stress reduction, sandslide algorithm, equivalent sand roughness and suspended transport load. The numerical results are sensitive to changes in the numerical model, and the most crucial parameters are the bed shear stress and the sandslide algorithm. The bed shear stress affected the maximum scour and the contour of the scour around the cylinder in different ways. The bed shear stress based on turbulent kinetic energy calculated a contour plot with a great fit to the experiment contour plot. Even if the contour had the right shape, the maximum scour depth would be high. The maximum scour depth can be adjusted with the critical Shields parameter. The numerical model was tested with the sandslide algorithms from Burkow [2010] and Wu [2007]. The result showed huge differences between the sandslide algorithms. The differences did not have a systematically context and acted differently in combination with other parameters.
The numerical model was examined with different diameters which calculated the same bed surface only on an enlarged scale. The effect of scour protection was shown to reduce the depth of scour.

6.2 Conclusions

Investigations with scour calculated with CFD require very small mesh sizes to obtain an accurate answer. The mesh size in the numerical model cannot be small enough

to get an accurate answer because the calculations demand a lot of computational power. Therefore, the model depends on approximations for solving scour investigations. The numerical model depends on choosing the correct approximations to obtain a good result. The chosen bed shear stress formulation is based on different approximations that influence the result. The velocity-based bed shear stress formulation calculated very high values for bed shear stress compared to the other formulations. The bed shear stress formulation based on turbulent kinetic energy calculates a more realistic scour hole because it has the most similar contour of the bed surface near the cylinder compared to the experiment. Bihs and Olsen [2011] found that the most suitable shear stress reduction for currents was Kovacs and Parker [1994] which is also valid for this model. The sandslide algorithm has a huge effect on the result. The sandslide algorithms from Burkow [2010] and Wu [2007] show different answers, and both models vary a lot when they are combined with other parameters. The sandslide algorithm from Burkow [2010] combined with the bed shear stress based on turbulent kinetic energy obtain the best contour shape of the scour compared to the experiment. The effect of adding suspended load is less scour depth. The suspended load contributes to backfilling of the scour hole.
The numerical model with larger diameter calculated the same scour shape on a larger scale. The maximum depth of the scour was much deeper. Scour protection resulted in less scour depth. The sediment transport model is not suitable for simulations with scour protection since the sediment transport model is based on formulas for sand. The consequence of the chosen numerical model was wrong edge scour around the scour protection.

6.3 Suggestions for further work

The parameter study has provided many benefits and limitations regarding the sediment transport model calculated in REEF3D::CFD. The model is very sensitive to changes in the numerical setup. The results from the different sandslide algorithms showed little consistent results. The sandslide algorithm makes the scour depth converge when the experimental result increases until the end. It would also be of interest to investigate the scour protection with a particle-based model. The advantage of a particle-based model is the ability to consider sediments in scour protection that are greater than sand. Suggestions for further work are summarized as follows:

- Investigate the sandslide algorithm in order to fit the inclination of the scour depth over time in the experiment.
- Investigate the scour protection with a particle-based model. The particle-based method allows us to examine the erosion of scour protection.

Bibliography

Ambitious offshore wind initiative, Government, No: 83/22, Date: 11/05/2022. URL https://www.regjeringen.no/en/aktuelt/ambitious-offshore-wind-power-initiative/id2912297/.

IEA (2021), Global Energy Review 2021, IEA, Paris. URL https://www.iea.org/reports/global-energy-review-2021.

Statnett (2021), Statnetts langtids markedsanalyse, LMA. URL https://www.statnett.no/globalassets/for-aktorer-i-kraftsystemet/planer-og-analyser/lma/2021-06-30-lma-oppdatering.pdf.

N. Ahmad, S. Afzal, H. Bihs, and Ø. A. Arntsen. Three-dimensional numerical modeling of local scour around a non-slender cylinder under varying wave conditions. In *36th IAHR World Congress*, 2015.

N. Ahmad, H. Bihs, D. Myrhaug, A. Kamath, and Øivind A. Arntsen. Three-dimensional numerical modelling of wave-induced scour around piles in a side-by-side arrangement. *Coastal Engineering*, 138:132–151, 2018. ISSN 0378-3839. doi: https://doi.org/10.1016/j.coastaleng.2018.04.016. URL https://www.sciencedirect.com/science/article/pii/S0378383917305604.

N. Ahmad, H. Bihs, D. Myrhaug, A. Kamath, and Arntsen. Numerical modelling of pipeline scour under the combined action of waves and current with free-surface capturing. *Coastal Engineering*, 148, 02 2019a. doi: 10.1016/j.coastaleng.2019.02.008.

N. Ahmad, H. Bihs, D. Myrhaug, A. Kamath, and Arntsen. Numerical modeling of breaking wave induced seawall scour. *Coastal Engineering*, 150:108–120, 2019b. doi: 10.1016/j.coastaleng.2019.02.008.

N. Ahmad, A. Kamath, and H. Bihs. 3d numerical modelling of scour around a jacket structure with dynamic free surface capturing. *Ocean Engineering*, 200:107104, 2020. ISSN 0029-8018. doi: https://doi.org/10.1016/j.oceaneng.2020.107104. URL https://www.sciencedirect.com/science/article/pii/S0029801818313647.

C. E. Arboleda Chavez, V. Stratigaki, M. Wu, P. Troch, A. Schendel, M. Welzel, R. Villanueva, T. Schlurmann, L. De Vos, D. Kisacik, F. Taveira Pinto, T. Fazeres-Ferradosa, P. Rosa Santos, L. Baelus, V. Szengel, A. Bolle, R. Whitehouse, and D. Todd. Large-scale experiments to improve monopile scour protection design adapted to climate change—the proteus project. *Energies*, 12(9), 2019. ISSN 1996-1073. doi: 10.3390/en12091709. URL https://www.mdpi.com/1996-1073/12/9/1709.

S. F. Ashby and R. D. Falgout. A parallel multigrid preconditioned conjugate gradient algorithm for groundwater flow simulations. *Nuclear Science and Engineering*, 124 (1):145–159, 1996. doi: 10.13182/NSE96-A24230.

C. Baykal, B. M. Sumer, D. R. Fuhrman, N. G. Jacobsen, and J. Fredsøe. Numerical investigation of flow and scour around a vertical circular cylinder. *Philosophical Transactions of the Royal Society A: Mathematical, Physical and Engineering Sciences*, 373(2033):20140104, 2015. doi: 10.1098/rsta.2014.0104. URL https://royalsocietypublishing.org/doi/abs/10.1098/rsta.2014.0104.

S. Beji and J. Battjes. Numerical simulation of nonlinear wave propagation over a bar. *Coastal Engineering*, 23(1):1 – 16, 1994. ISSN 0378-3839. doi: https://doi.org/10.1016/0378-3839(94)90012-4. URL http://www.sciencedirect.com/science/article/pii/0378383994900124.

S. Beji and J. A. Battjes. Experimental investigation of wave propagation over a bar. *Coastal Engineering*, 19(1-2):151–162, 2 1993. ISSN 03783839. doi: 10.1016/0378-3839(93)90022-Z.

H. Bihs. *Three-dimensional numerical modeling of local scouring in open channel flow*. PhD thesis, Department of Hydraulic and Environmental Engineering, NTNU Trondheim, 2011.

H. Bihs and N. R. B. Olsen. Numerical modeling of abutment scour with the focus in the incipient motion on sloping beds. *Journal of Hydraulic Engineering*, 137(10): 1287–1292, 2011.

H. Bihs, A. Kamath, M. Alagan Chella, A. Aggarwal, and A. Arntsen. A new level set numerical wave tank with improved density interpolation for complex wave hydrodynamics. *Computers and Fluids*, 140:191–208, 11 2016. ISSN 00457930. doi: 10.1016/j.compfluid.2016.09.012.

B. Brørs. Numerical modeling of flow and scour at pipelines. *Journal of Hydraulic Engineering*, 125(5):511–523, 1999. doi: 10.1061/(ASCE)0733-9429(1999)125:5(511).

M. Burkow. Numerische simulation stromungsbedingten sedimenttransports und der entstehenden gerinnebettformen. *Master's thesis, Mathematisch-Naturwissenschaftlichen Fakultat der Rheinischen Friedrich-Wilhelms-Universitat Bonn, Bonn, Germany*, 2010.

L. Chen, J. Zang, A. Hillis, G. Morgan, and A. Plummer. Numerical investigation of wave–structure interaction using openfoam. *Ocean Engineering*, 88:91–109, 2014. ISSN 0029-8018. doi: https://doi.org/10.1016/j.oceaneng.2014.06.003. URL https://www.sciencedirect.com/science/article/pii/S0029801814002169.

A. Chorin. Numerical solution of the Navier-Stokes equations. *Mathematics of Computation*, 22:745–762, 1968.

S. Dey. Experimental studies on incipient motion of sediment particles on generalized sloping fluvial beds. *Journal of Sediment Research*, 16(3):391–398, 2001.

S. Dey. Threshold of sediment motion on combined transverse and longitudinal sloping beds. *Journal of Hydraulic Research*, 41(4):405–415, 2003.

P. A. Durbin. INVITED REVIEW: Limiters and wall treatments in applied turbulence modeling. *Fluid Dynamics Research*, 41(1):012203, Feb. 2009. doi: 10.1088/0169-5983/41/1/012203.

F. Engelund and J. Fredsøe. A Sediment Transport Model for Straight Alluvial Channels. *Hydrology Research*, 7(5):293–306, 10 1976. ISSN 0029-1277. doi: 10.2166/nh.1976.0019. URL https://doi.org/10.2166/nh.1976.0019.

J. Fredsoe and R. Deigaard. *Mechanics of coastal sediment transport*, volume 3. World scientific publishing company, 1992.

D. Fuhrman, C. Baykal, B. Sumer, N. Jacobsen, and J. Fredsoe. Numerical simulation of wave-induced scour and backfilling processes beneath submarine pipelines. *Coastal Engineering*, 94:10–22, 12 2014. doi: 10.1016/j.coastaleng.2014.08.009.

M. Griebel, T. Dornseifer, and T. Neunhoeffer. *Numerical Simulation in Fluid Dynamics, a Practical Introduction*. SIAM, 1998.

J. N. Hunt and C. C. Inglis. The turbulent transport of suspended sediment in open channels. *Proceedings of the Royal Society of London. Series A. Mathematical and Physical Sciences*, 224(1158):322–335, 1954. doi: 10.1098/rspa.1954.0161. URL https://royalsocietypublishing.org/doi/abs/10.1098/rspa.1954.0161.

N. G. Jacobsen, D. R. Fuhrman, and J. Fredsøe. A wave generation toolbox for the open-source CFD library: OpenFOAM. *International Journal for Numerical Methods in Fluids*, 70(9):1073–1088, 2012.

G. S. Jiang and C. W. Shu. Efficient implementation of weighted ENO schemes. *Journal of Computational Physics*, 126:202–228, 1996.

A. Khosronejad, S. Kang, I. Borazjani, and F. Sotiropoulos. Curvilinear immersed boundary method for simulating coupled flow and bed morphodynamic interactions due to sediment transport phenomena. *Advances in Water Resources - ADV WATER RESOUR*, 34:829–843, 07 2011. doi: 10.1016/j.advwatres.2011.02.017.

A. Kovacs and G. Parker. A new vectorial bedload formulation and its application to the time evolution of straight river channels. *Journal of Fluid Mechanics*, 267: 153–183, 1994.

F. Li and L. Cheng. Prediction of lee-wake scouring of pipelines in currents. *ASCE Journal of Waterway, Port, Coastal, and Ocean Engineering*, 127(2):106–112, 2001. ISSN 0733-950X. doi: 10.1061/(ASCE)0733-950X(2001)127:2(106).

D. Liang and L. Cheng. Numerical model for wave-induced scour below a submarine pipeline. *Journal of Waterway Port Coastal and Ocean Engineering-asce - J WATERW PORT COAST OC-ASCE*, 131, 09 2005. doi: 10.1061/(ASCE) 0733-950X(2005)131:5(193).

O. Link. Untersuchung der kolkung an einem schlanken zylindrischen pheiler in sandigem boden. *PhD thesis. Institut fr Wasserbau und Wasserwirtschaft, Technische Universitt Darmstadt*, 2006. URL https://ci.nii.ac.jp/naid/10028163165/en/.

M.-M. Liu, L. Lu, B. Teng, M. Zhao, and G. qiang Tang. Numerical modeling of local scour and forces for submarine pipeline under surface waves. *Coastal Engineering*, 116:275–288, 2016. ISSN 0378-3839. doi: https://doi.org/10.1016/j.coastaleng.2016.05.003. URL https://www.sciencedirect.com/science/article/pii/S0378383916300722.

X. Liu and M. H. García. Three-dimensional numerical model with free water surface and mesh deformation for local sediment scour. *Journal of Waterway, Port, Coastal, and Ocean Engineering*, 134(4):203–217, 2008.

A. P. S. C. C. P. S. B. N. C. Y. C. L. G. M. G. M. H. K. L. E. L. J. M. T. M. T. W. O. Y. R. Y. Masson-Delmotte, V.P. Zhai and B. Z. (eds.). Climate Change 2021: The Physical Science Basis. 2021.

N. R. B. Olsen and H. M. Kjellesvig. Three-dimensional numerical flow modelling for estimation of maximum local scour depth. *IAHR Journal of Hydraulic Research*, 36(4):579–590, 1998.

N. R. B. Olsen and M. C. Melaaen. Three-dimensional calculation of scour around cylinders. *Journal of Hydraulic Engineering*, 119(9):1048–1054, 1993.

S. Osher and J. A. Sethian. Fronts propagating with curvature-dependent speed: Algorithms based on Hamilton-Jacobi formulations. *Journal of Computational Physics*, 79:12–49, 1988.

D. Peng, B. Merriman, S. Osher, H. Zhao, and M. Kang. A PDE-based fast local level set method. *Journal of Computational Physics*, 155:410–438, 1999.

A. Roulund, B. M. Sumer, J. Fredsøe, and J. Michelsen. Numerical and experimental investigation of flow and scour around a circular pier. *Journal of Fluid Mechanics*, 534:351–401, 2005.

G. Seminara, L. Solari, and G. Parker. Bed load at low shields stress on arbitrarily sloping beds: Failure of the bagnold hypothesis. *Water resources research*, 38(11): 31–1, 2002.

A. Shields. Anwendungen der Ähnlichkeitsmechanik und der turbulenzforschung auf die geschiebebewegung, 1936.

C. W. Shu and S. Osher. Efficient implementation of essentially non-oscillatory shock-capturing schemes. *Journal of Computational Physics*, 77(2):439–471, 8 1988. ISSN 10902716. doi: 10.1016/0021-9991(88)90177-5.

B. M. Sumer, J. Fredsøe, and N. Christiansen. Scour around vertical pile in waves. *Journal of Waterway, Port, Coastal, and Ocean Engineering*, 118(1):15–31, 1992. doi: 10.1061/(ASCE)0733-950X(1992)118:1(15).

M. Sussman, P. Smereka, and S. Osher. A level set approach for computing solutions to incompressible two-phase flow. *Journal of Computational Physics*, 114:146–159, 1994.

M.-H. Tseng, C.-L. Yen, and C. Song. Computation of three-dimensional flow around square and circular piers. *International Journal for Numerical Methods in Fluids*, 34:207 – 227, 10 2000. doi: 10.1002/1097-0363(20001015)34:3⟨207::AID-FLD31⟩3.0.CO;2-R.

H. A. van der Vorst. Bi-CGSTAB: A Fast and Smoothly Converging Variant of Bi-CG for the Solution of Nonsymmetric Linear Systems. *SIAM Journal on Scientific and Statistical Computing*, 13(2):631–644, 3 1992. ISSN 0196-5204. doi: 10.1137/0913035. URL https://epubs.siam.org/page/terms.

L. C. van Rijn. Sediment transport, part i: Bed load transport. *Journal of Hydraulic Engineering*, 110(10):1431–1456, 1984. doi: 10.1061/(ASCE)0733-9429(1984)110:10(1431).

L. C. van Rijn. Sediment transport, part ii: Suspended load transport. *Journal of Hydraulic Engineering*, 110(11):1613–1641, 1984b.

L. C. van Rijn. Principles of sediment transport in rivers, estuaries and coastal seas. 1993.

D. C. Wilcox et al. *Turbulence modeling for CFD*, volume 2. DCW industries La Canada, CA, 1994.

W. Wu. *Computational river dynamics*. Crc Press, 2007.

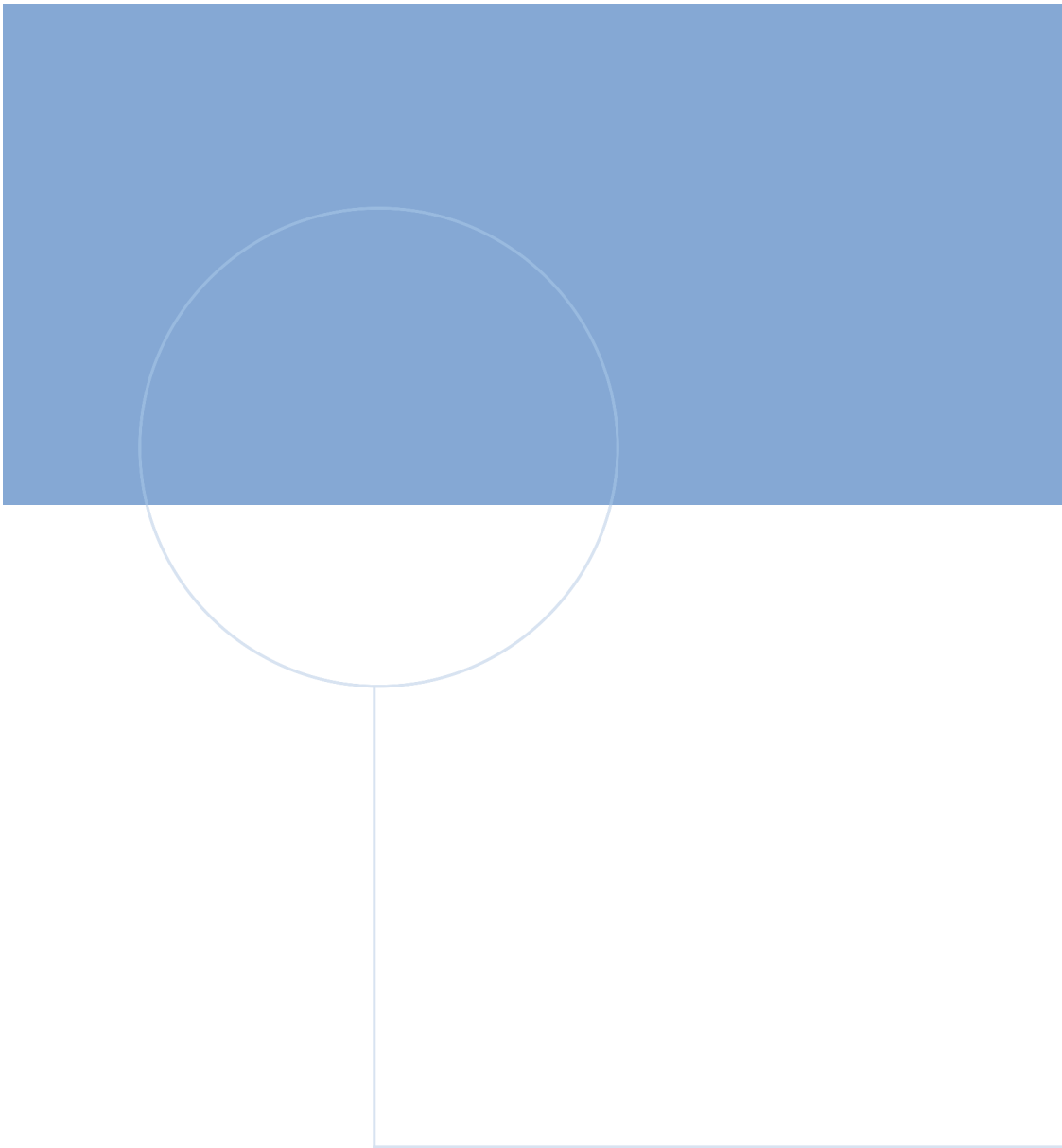

NTNU

Norwegian University of
Science and Technology